PREDICTION AND OPTIMIZATION OF THE MECHANICAL PERFORMANCE OF 2D MATERIALS KIRIGAMI: MOLECULAR DYNAMICS SIMULATION COMBINED WITH MACHINE LEARNING

by

SHAOHENG LI

(Under the Direction of Xianqiao Wang)

## ABSTRACT

I develop a generic coarse-grained potential in order to study the mechanical performance of 2D materials-based cellular kirigami structures towards understanding of the relationship between mechanical properties, structure pattern, and component material. Results indicate that there are two distinct stress-strain stages, J-shape non-linear elasticity and linear elasticity, determined by the material structure density. Moreover, hole-in structures show a better performance over no-hole structures for ductility. In addition, the material effect on the mechanical performance of 2D materials-based cellular kirigami is significant, exemplified by graphene-based structures outperforming those composed of other 2D materials. Furthermore, by integrating coarse-grained molecular dynamics (CGMD) simulations with machine learning algorithms, the mechanical performance of 2D materials-based kirigami structures with mixed cellular patterns can be predicted in order to optimize the design patterns of the kirigami structures. CGMD simulation are performed to obtain stress-strain responses of the $3 * 3$ grid architectured graphene kirigami under

biaxial tensile tests, in which 2,483 datasets are obtained with different combinations of cellular patterns. With previous stress-strain responses, feedforward neural networks (FNN) have been applied in order to obtain prediction of mechanical performance. Result shows the R2 were able to increase up to 0.4 by optimizing the structure of the input dataset, which revealed the possibility of using machine learning method to design and predict mechanical properties of architectured 2D materials, it also specifically demonstrated that FNN could achieve an acceptable accuracy in terms of prediction by increasing the structural details and size of the training dataset . Overall, this study provides a computational basis towards the predictive design of future kirigami structures with outstanding properties and functions.

INDEX WORDS: molecular dynamics, kirigami, machine learning

# PREDICTION AND OPTIMIZATION OF THE MECHANICAL PERFORMANCE OF 2D MATERIALS KIRIGAMI: MOLECULAR DYNAMICS SIMULATION COMBINED WITH MACHINE LEARNING

by

SHAOHENG LI

B.S., HENAN UNIVERSITY, CHINA, 2018

A Thesis Submitted to the Graduate Faculty of the University of Georgia in Partial Fulfillment of the Requirements for the Degree

MASTER OF SCIENCE

ATHENS, GEORGIA

2020

# PREDICTION AND OPTIMIZATION OF THE MECHANICAL PERFORMANCE OF 2D MATERIALS KIRIGAMI: MOLECULAR DYNAMICS SIMULATION COMBINED WITH MACHINE LEARNING

by

SHAOHENG LI

| | |
|---|---|
| Major Professors: | Xianqiao Wang |
| Committee: | Ramana M Pidaparti |
| | Mi geum Chorzepa |

Electronic Version Approved:

Ron Walcott
Dean of the Graduate School
The University of Georgia
December 2020

# ACKNOWLEDGEMENTS

I would like to first express my deepest gratitude to my advisor Dr. Xianqiao Wang. Without his unending faith in my potential and his wonderful and tireless guidance none of my success could have been possible.

My thanks to Dr. Ramana M. Pidaparti, not only for serving on my graduate committee, but also for his significant contribution to my education and his generous support during times of need.

I would also like to thank Dr. Mi geum Chorzepa for serving on my graduate committee and for her support throughout my studies.

My fellow graduate students Dr. Ning Liu, Mr. Matthew Becton, and Mr. Nicholas Winter have also played a major role, and their assistance has been a great help to me.

I must also thank Ms. Margaret Sapp. Her constant assistance with the many matters pertaining to registration and graduation. Without her assistance I would never have made it through my master's degree.

TABLE OF CONTENTS

LIST OF FIGURES

LIST OF TABLES

# CHAPTER1 INTRODUCTION AND LITERATURE REVIEW

## 1.1 A brief history of 2D nanomaterials

Since ancient times, the improvement of materials has been an essential basis for human survival and development, and the history of human development is also the evolutionary history of materials. With recent developments in science and technology, human being has entered the age of nanomaterials. The technological revolution brought about by new nanomaterials will have a profound impact on human society[1].

Materials are normally classified according to their structure or properties. Nanomaterials are a type of material that have at least one dimension less than 100nm and can have much different physical properties when compared with so-called 'bulk' materials. According to the dimensions of the material, it can be divided into three categories: zero-dimensional atomic clusters or nanocage structures; one-dimensional nanowires or nanotubes, such as silicon nanowires[2], carbon nanotubes[3], and similar; and two-dimensional nanosheets, such as graphene[4], silicene[5], and similar. Each type of nanomaterial has attracted wide attention from researchers, and each have their own unique characteristics. One of the most intriguing properties of two-dimensional nanosheets is its large specific surface area (SSA), which determines the surface chemical activity of the material. A very large SSA is one of the reasons why so much interest is focused on graphene[6]. It is expected that catalytic materials with high specific surface area will have huge application prospects[6]. In addition to the huge specific surface area, the surface atom coordination of nanomaterials is insufficient due to the lack of bulk material on either side, making these surface atoms easy to

combine with other foreign atoms, making for excellent gas adsorbent materials[6]. In terms of optics, as opposed to conventional bulk materials, single-layer two-dimensional nanomaterials have a range of absorption effects on electromagnetic waves and can be used as both invisible materials and radiation shielding materials[4]. The size effect, which expands the application range of nano-optoelectronic materials, has important practical significance in optical applications. In terms of magnetism, the giant magnetoresistance effect in the layered film structure was first discovered in late 1980s[7]. Research shows that the resistance value of the giant magnetoresistive material is related to the magnetization direction of the ferromagnetic material thin film layer, and the resistance value of the two layers of magnetic material when the magnetization directions are opposing is significantly greater than the resistance value when the magnetization directions are the same[7, 8]. In addition, magnetoelectronics is a new cross-effect of magnetism and electricity in nanoscale materials[8]. The direction of electron spin will affect the transport properties of the material. As an important part of nanoelectronics, magnetoelectronics has a wide range of applications in the fields of magnetic recording, non-volatile information storage, spin transistors and quantum computers[8].

Although for a long time the research community believed that two-dimensional (2D) crystals may not be stable experimentally, Novosolev, Geim, and colleagues[4] demonstrated for the first time the isolation of single-atom-thick carbon sheets in 2004, which is termed graphene. This discovery inspired physicists, chemists, and even circuit designers around the world to develop new ideas using carbon-based electronics. In the past few years, many applications related to graphene have been developed and are likely to be industrialized in the near future[9, 10] (Figure1-1). Some promising applications include RF electronics[11], advanced sensors[12], translucent electrodes and

electronics[13], low-power switches[14], solar cells[15], battery energy storage[16], and adjustable plasma devices for terahertz[17] and mid-infrared applications.

Recently, 2D materials provide a new ideal world for creation and innovation. The unique properties of 2D materials have attracted a wide range of research activities to use this new material system to improve existing electronics, optoelectronics[18], and sensing applications[18], as well as invent new applications. From a mechanical point of view, crystalline two-dimensional materials[19] can withstand more than 10% in-plane deformation strain before fracture, which is an order of magnitude higher than the deformation of a typical bulk semiconductor whose fracture value is usually <1%[19]. The inherently high flexibility, in-plane as well as out-of-plane, has also stimulated great efforts to further control and modulate the electrical and optical properties of 2D semiconductors through strain engineering[19]. Various methods can be used to further improve the mechanical properties of two-dimensional materials, and even optimize specific mechanical properties as needed.

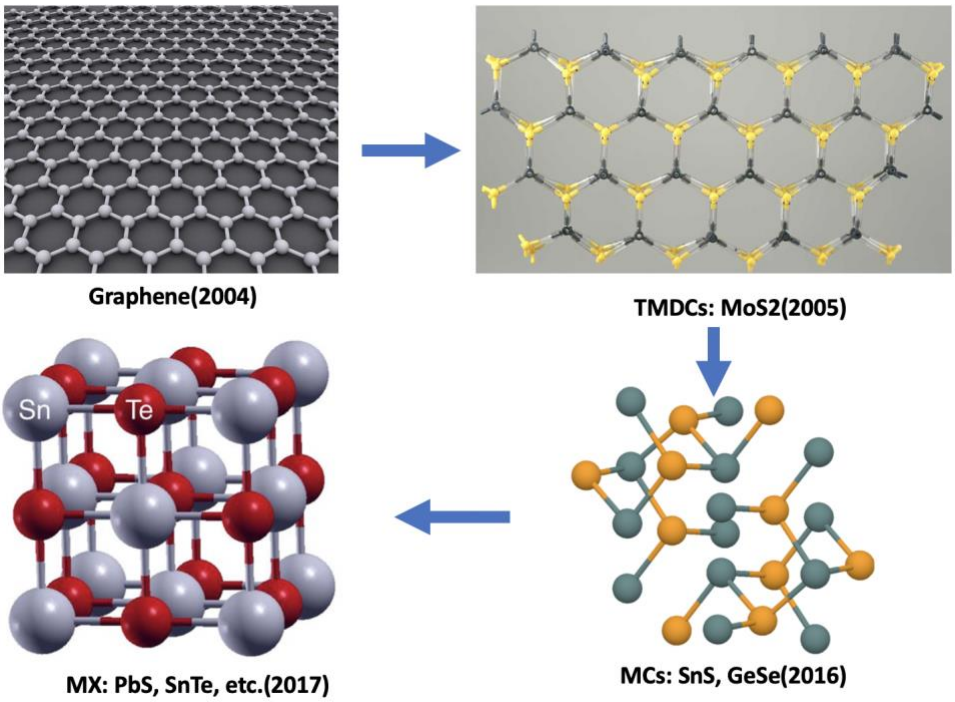


**Figure 1-1** The emergence of new classes of 2D nanomaterials

### 1.2 2D materials kirigami

Techniques to combine the application of paper-cutting technology with two-dimensional materials is a natural evolution of two-dimensional nanomaterials design. The novel innovation in Ortrud Medical's tourniquet design is the use of a Kirigami 'pattern', a Japanese paper art involving cutting and folding, to reduce the resistive force of the 2D material[20]. Moreover, it can be used to alter the properties of a sheet of 2D material and turn it into a metamaterial – a material engineered to produce properties which do not occur naturally. Mechanical properties of kirigami-enhanced materials such as the stiffness and Poisson's ratio can be changed by altering cut lengths or patterns[20]. In addition, patterned defects can also be used to change the material properties of a 2D sheet in 3 dimensions – such as increasing the buckling stiffness[21].

A lot of effort has been put towards research into kirigami materials, in which different designs are proposed to achieve exceptional auxetic mechanical properties, such as negative Poisson's

ratio[22, 23], negative stiffness[24, 25], outstanding stretchability[23, 26, 27], *etc*. For example, Liu *et al.* has adopted a sinusoidal cutting pattern for kirigami based on 2D materials, in which the auxeticity can be systematically tuned by geometrical parameters of cutting patterns and mechanical anisotropy of base materials.[23] Timothy *et al.* proposed a design utilizing buckling of small-scale structural elements, which can achieve a negative stiffness for kirigami materials.[25] Rogers and Huang *et al.* have proposed multiple designs of 2D kirigami structures which can form different targeted 3D morphologies through out-of-plane buckling.[28] Xu *et al.* proposed two theoretical models based on continuum mechanics to predict the elastic properties of architected heterogeneous 2D structures, and thus promoted the search for novel architected 2D structures with exceptional mechanical performance.[29 30]

Along with the great advances witnessed in both theoretical and experimental researches of 2D kirigami, plenty of cutting patterns have been proposed to design architected 2D structures with targeted mechanical properties. Through combining different cellular cutting patterns, 2D kirigami materials can be designed with systematically tunable mechanical performance.[30-34] In addition to assembly of cellular cutting patterns, manipulation of bonding connections between adjacent cutting units is also critical for altering material performance and developing new functionalities for 2D material kirigami.[35-37] Despite the successful designs proposed above, the fundamental physics of those designing strategies remains an open question. In this case, machine learning algorithms can serve as a powerful tool to establish a solid connection between cutting patterns and mechanical performance for 2D kirigami material without enough prior knowledge of relevant physics, which will be discussed in the section below.

### 1.3 Machine learning of architected 2D structure.

Typically, it will take between ten and twenty years of study on nanomaterials from the initial investigation to the first application. The most traditional method for studying nanomaterials is experimental exploration. Experimental measurement usually includes structure synthesis, microstructure property analysis, and property measurement[38]. Experimental studies can often take a very long time but can be considered the simplest and most accurate method to study materials. However, this method has high requirements for equipment, experimental environment, and the professional knowledge of researchers. These requirements are greatly affected by the external environment, experimental period, and budget, which make it difficult to accelerate the development of nanomaterials. As another option, the rise of computational chemistry has become a powerful tool for studying nanomaterials. High-precision computation[39] methods such as DFT-based electronic structure calculations[40], molecular dynamics (MD) simulations[41], Monte Carlo simulations[42], phase field methods[43], and continuous macroscopic methods[44] are currently widely used in the discovery of new materials. Although theoretical computation requires experimental verification, it greatly shortens the tedious process of experiments and provides beneficial guidance for further study. However, the high-precision computation method requires high-performance computing equipment, plus the limitation of running on large-scale computing cluster, which prevent this method from being widely used.

In view of the limitations of the above nanomaterial design and property prediction methods, machine learning is a powerful solution. Computers can use pre-developed algorithms to learn data by simulating the linear or nonlinear relationship between material properties and related variables[38]. Machine learning extracts knowledge from existing results to gain insights, then produces reliable and repeatable decisions and results. Its adaptability to the classification and

regression problems of high-dimensional data has seen it playing an important role in speech recognition, image recognition, image classification, bioinformatics, drug discovery, customized advertising, and video recommendations[38]. The pioneering application of machine learning in materials science can be traced back to the 1990s[45], when machine learning methods such as symbolic methods and artificial neural networks (ANNs) were used to predict the tensile strength and compression strength of the fiber/matrix interface in ceramic matrix composites, and very good results have been achieved[45]. Since then, machine learning has been used to solve various problems in materials science.

Generally ,the modeling establishment of machine learning in materials science can be divided into three steps: sample establishment, model construction, and model evaluation[38]. The sample establishment can be divided into two parts: the preprocessing of raw data, and the selection of descriptors. The original data are generally obtained from computational simulations and experimental measurements[38]. These data are usually incomplete, noisy, or inconsistent. Therefore, the original data needs to be preprocessed when constructing a sample. In addition, the type and number of descriptors have even a greater impact on the results of the model, and it is likely that some of the descriptors are not related to the target properties, or the correlation between the descriptors is too strong, so it is necessary to filter the descriptors. The model establishment is essentially a black box that uses linear or non-linear functions to associate input data with target properties. In materials science research, there are often complicated relationships between descriptors and target properties, which cannot be solved well by traditional methods. However, machine learning can find a specific mapping function to achieve as close as possible the objective function coefficients, which can be well applied to the solution of these problems. Model evaluation can tell whether a data-driven model not only performs well on existing data, but also

performs well on unknown data. Usually the selected data set is divided into a training set and a test set, and the generalization error of the model is evaluated based on the prediction of the test set. Therefore, it is necessary to select the appropriate algorithm for the training process. Different algorithms have different prediction accuracy and generalization ability for the same problem. Each algorithm has its own application range, and there is no algorithm suitable for all problems. Machine learning algorithms commonly used in materials science can be divided into four categories: regression, classification, clustering, and probability estimation.[38] Regression, clustering and classification algorithms are mainly used to predict the properties of materials at the macro and micro levels.[45] The probability estimation algorithm is mainly used to discover new materials. The material properties predicted by machine learning mainly involve band gap, formation energy, lattice thermal conductivity, magnetism, elastic constant, melting point, gas adsorption capacity, etc. The basic steps of using machine learning to predict the properties of materials can be summarized into three steps. First, the data of the research system is processed and the features related to the predicted target properties are selected. Then, the mapping relationship between the selected features and the target properties is found through the training model, and the prediction ability and generalization ability of the model are evaluated. Finally, the best model is selected to predict the properties of unknown compounds. The predictive ability depends largely on the selected machine learning algorithm and sample construction, which means no model can be applied to all systems. Therefore, in order to find the best one, it is necessary to compare different machine learning models based on different algorithms.

### 1.4 Contributions of this thesis

Considering the representative role of graphene in two-dimensional materials, this work will study the mechanical properties of graphene-based cellular kirigami structures, which may also help to

study multiple other applications of 2D materials due to the exceptional transferability of the developed force-field potential. First, investigations will be performed into how to enhance the mechanical properties of 2D materials by using different kirigami structures and the effects of structure and unit cell parameters. Then, machine learning will be applied to study the designed architectured 2D materials. This paper will be organized as follows: Chapter 2 will present a computational study of 2D materials kirigami. Chapter 3 will further discuss details of architectured structure and its mechanical property prediction by machine learning algorithm. Chapter 5 will summarize the findings and conclude this thesis.

# CHAPTER2 MECHANICS OF 2D MATERIALS BASED CELLULAR KIRIGAMI STRUCTURES: A COMPUTATIONAL STUDY[1]

[1]Shaoheng Li*, Ning Liu, Matthew Becton, Nicholas Winter, Ramana M. Pidaparti, Xianqiao Wang, 2020, "Mechanics of 2D materials based cellular kirigami structures: A computational study", JOM. Reprinted here with permission of publisher.

**ABSTRACT**

In this paper, I develop a generic coarse-grained potential for a general group of 2D materials to study the mechanical performance of 2D materials-based cellular kirigami structures for understanding of the relation between mechanical properties and structure pattern as well as the material component. By patterning the structure lattice cell, the mechanical properties of 2D materials-based structures show a very wide range from almost zero to those of the pristine 2D materials by orders of magnitude. Moreover, results indicate that there are two distinct stress-strain stages associated with density, J-shape non-linear, and linear elasticity. Results also indicate that hole-in structures show a better performance over no-hole structures on ductility. In addition, the material effect on mechanical performance of 2D materials-based cellular kirigami is significant, exemplified by graphene-based structure outperforming those made of other 2D materials. Overall, this study provides a computational basis towards designing future kirigami structures with outstanding properties and functions.

## 2.1. Introduction

Currently, due to the unique transformation characteristics such as twisting and rotation, 2D materials with reasonable designed 2D structures have shown a wealth of unique mechanical properties, such as tensile strength, toughness, and stiffness, as well as the ability for shape reconfiguration[30]. These extraordinary properties are usually governed by the structure[30]. However, it is still an open question of how the material composition influences the exceptional properties aforementioned. Thus, it would be interesting to explore if component material with outstanding mechanical properties, such as 2D Materials[46], can help improve the emerging extraordinary properties of architected 2D structures. In the previous studies, along with the prosperity of 2D materials, rationally designed 2D structures have attracted enormous interest for applications in flexible and stretchable electronics[47-49], phononic devices[50], and structurally tunable optical[51]. Despite the experimental achievements, the combined effect of cellular structure and component material on mechanical performance of architected structures based on 2D materials have not been thoroughly understood. Therefore, in this paper, mechanical performance of 2D material-based cellular kirigami structures will be investigated to establish such a link between nanoscale characteristics and macroscopic performance.

Kirigami, a term taken from the Japanese art of cutting paper, due to the principles of classical elasticity, it is anticipated that increasing cuts (i.e., removing atoms) will both weaken and soften the material in most cases[52]. In principle, the elastic properties of the sheet materials are able to be designed and controlled in a highly flexible manner by this approach. So far, the kirigami approach has been successfully applied to improve the stretchability of 2D materials[27], and examples of the structural and geometric diversity that can be achieved using kirigami approaches for 2D materials

have already been demonstrated experimentally. For example, Qi *et al.*[27] verified that the yield strain of $MoS_2$ increased fourfold, and the fracture strain of graphene was enhanced about three times by kirigami approach[27, 53].The fracture strain of hexagonal boron nitride kirigami structures increased three to five times compared to the original 2D material[27, 53]. However, the exact relationship between the structures of kirigami 2D materials and their mechanical properties is still an open question. Unlike macroscopic kirigami, which is able to be directly achieved by cutting flat sheets (e.g. paper) and manually transforming the sheets into desired shapes, 2D material kirigami in microscopic scales is challenging because of the limitation in finding a micro-/nanomanipulator which is advanced enough to perform the desired carefully dictated steps necessary for the process[54]. Moreover, due to the limited resolution of current experimental techniques at the nanoscale, it is difficult to study the knowledge of molecular scale processes.[55] Therefore, in order to efficiently study different 2D materials and acquire a comprehensive understanding of 2D materials-based kirigami characteristics, a computational model both physically accurate and computationally efficient is needed.

All-atom molecular dynamics (AAMD) simulation and theoretical modeling can serve as useful tools to study the phenomena of 2D materials at the nanoscale, also helps to interpret experimental data, such as transition from J-shaped nonlinear elasticity to linear elasticity.[56, 57] Therefore, most pervious researches on 2D materials simulation were performed by AAMD simulations.[58] Despite the tremendous success of these investigations, AAMD still has some drawbacks. In most cases, the system box sizes of the simulation of 2D materials-based systems is less than $10\ nm$ per dimension, which requires extremely high computational power[58]. Therefore, it is outrageously expensive to study the failure modes and failure mechanisms of 2D materials by AAMD simulations[55, 58], thus restricting the understanding of the properties of 2D materials based kirigami.

In order to solve these drawbacks, coarse-grained molecular dynamics (CGMD) models would be an ideal choice for simulations due to its high computational efficiency and physical accuracy. CGMD model allows each CG bead to represent dozens of atoms, which significantly lowers the degrees of freedom of the atoms.[56, 59] Therefore, CGMD simulations are able to carry out simulations of 2D materials several hundred times faster than AAMD simulations with alike precision. [59, 60].To date, there are several CG models that have been developed to simulate the mechanics of 2D materials, such as graphene, graphene oxide, and phosphorene[55, 58, 60, 61]. Most of those models have a fine coarse-graining mapping (four atoms to one CG bead), which enables it a good physical accuracy [55, 58, 60]. In addition, the temporal scale these models can reach is significantly enhanced. For example, the timestep for the CG model of graphene by Luis *et al*. can be up to 7.6 fs, which is much greater than 1 fs in AAMD. Despite the extended temproal and spatial scale, the existing CG models can hardly reach micrometer in length and microseconds in time, making it hard to establish a link between experiments and theories. Moreover, the poor transferability of the above models prohibits their applications for a general group of 2D materials. Therefore, it is necessary to develop a generic CG model for a general group of 2D materials with a highly coarser mapping, which could help reach a significantly greater temporal and spatial scale. This work will establish a CG model to study the mechanical properties of 2D materials-based cellular kirigami structures, which may also help to study multiple other applications of 2D materials due to the exceptional transferability of the developed force-field potential. Here, I will investigate how to enhance the mechanical properties of 2D materials by using different kirigami structures and the effects of structure and unit cell parameters. My paper will be organized as follows: Section 2 will discuss the CG model development and simulation set-up of this paper; Section 3 will focus on the analysis of mechanical behaviors of 2D material-based cellular kirigami

structures under uniaxial tension, in order to explore the relation between mechanical performance and structure pattern as well as material type; Section 4 will summarize the findings and conclude this paper.

## 2.2. Models and methods

### 2.2.1. Model setup

In this study, I introduce and set my focal investigation on five distinct 2D materials based kirigami cells. These basic cells are four-node structures with rationally designed architectures. When a uniaxial tensile stress $\sigma_x$ is applied to a cell, nonuniform stresses will appear due to the deformation heterogeneity with structure being contractile or auxetic. From the geometric parameters shown in Figure 2-1a, $d$ is the width of the structural ligands; $L$ is the length of the bridges. $L$ is fixed as $0.5\ a_0$ and due to the limitation of the structural integrities of different structures $d$ varies from a minimum of $4\ a_0$ to a maximum based on cell shape. The width of the bridge changes as the width of the ligand changes. The base unit termed $a_0$ is equal to a length of 2.5 nm. For the octagonal cell, $d$ varies from $4a_0$ to $28a_0$. For the star-shaped cell, $d$ varies from $4a_0$ to $14\ a_0$. For the fan-shaped cell, $d$ varies from $4a_0$ to $14a_0$. For the bent-cross cell, $d$ varies from $4a_0$ to $18a_0$. Finally, for the sinusoidal cell, the width $d$ varies from $4a_0$ to $28a_0$. All the cells are designed using my in-house code written in MATLAB before being exported to LAMMPS for simulation (further details below).

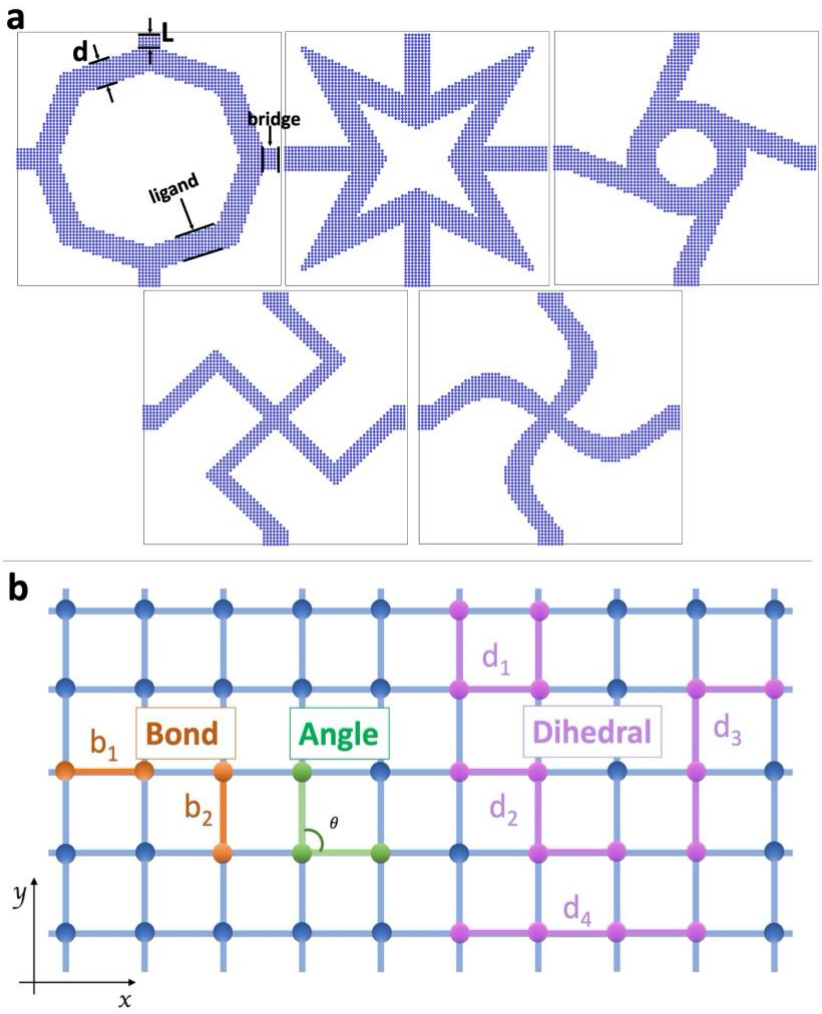


**Figure 2-1** (a) Overall view of five kirigami models, namely octagon, star-shape, san-shape, bent-cross, sinusoid. (b) CG model schematics. Illustration of the contributions of the CG force-field to the potential energy of the system. The CG lattice is shown in blue and the different interactions are highlighted with ball-stick representations in different colors. The distance between each mesoscale particle is $r_0 = 25Å$, where each particle effectively describes the behavior of approximately 250 atoms per monolayer.

### 2.2.2. CGMD model parameters, force field development, and validation

Here I developed a square coarse-grained model. Although the most 2D materials are of hexagonal symmetry, such as graphene and silicene, they are highly mechanical anisotropic along the zigzag and armchair directions. Also, the mechanical properties along these two directions holds the key to the design and development of 2D materials-based devices. The square coarse-grained lattice is a simple but generic model to well capture the mechanical anisotropy in 2D materials. Specifically, one of the advantages of this generic CGMD model is that the mechanical properties along the

lattice edge directions can be tuned through varying the interaction parameters, like the stiffness of the $b_1$ and $b_2$ bonds in Figure 2-2, in a decoupled manner, therefore offering a robust way to represent different kinds of 2D materials with widely varied and anisotropic mechanical properties.

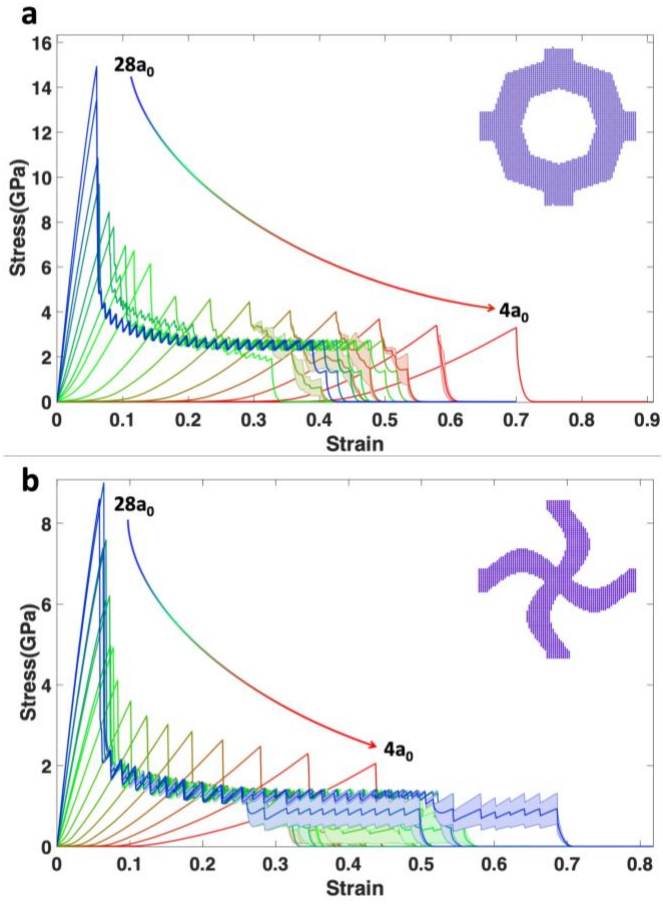


**Figure 2-2** (a) The stress-strain curve for octagonal cell based on graphene. (b) The stress-strain curve for sinusoidal cell based on graphene. (The width increases by 2a0 from 4a0 to 20a0, and the width increase by 1a0 from 20a0 to 28a0. As it can be seen from the curve, the tensile strength increases dramatically. Therefore, to well describe the relationship between strength and density, I add more data points from 20a0 to 28a0; The stress-strain curve for other cells are given in supplementary material Figure A-5)

The CGMD model's potential field can be divided into four parts: bonds, angles, dihedrals, and non-bonded interactions (Figure 2-1b)[55].The sum of potential energy ($U_{pot}$) can thus be expressed as:

$$U_{pot} = U_b + U_a + U_d + U_{nb} \tag{2.1}$$

where $U_b$ is the elastic energy from in-plane bond stretching, $U_a$ is the elastic energy from in-plane angle bending , $U_d$ is the elastic energy from out-of-plane dihedral bending, $U_{nb}$ is the elastic energy from non-bonded interactions. [55, 61]

For the bonded interactions, a Morse potential is implemented for axial stretching:

$$U_b = D[1 - e^{-\alpha(r-r_0)}]^2 \tag{2.2}$$

where $D$ is the parameter governing the depth of the potential well of the bond, $\alpha$ governs the width of the potential well of the bond, and $r_0$ is the equilibrium distance of the bond.

For 3-body (angle) interactions, a harmonic spring potential is implemented for shear deformation and out-of-plane bending, given by:

$$U_a = K_a[\theta - \theta_0]^2 \tag{2.3}$$

where $K_a$ is the spring constant of the angle interactions, and $\theta_0$ is the equilibrium angle.

For 4-body (dihedral) interactions, a cosine potential was used, given by:

$$U_d = K_d[1 - cos(2\phi)] \tag{2.4}$$

where $K_d$ is the spring constant of the dihedral interactions.

I use a Lennard-Jones potential to describes non-bonded interactions:

$$U_{nb} = 4\epsilon\left[\left(\frac{\sigma}{r}\right)^{12} - \left(\frac{\sigma}{r}\right)^{6}\right] \qquad r < r_c \tag{2.5}$$

Here, $\epsilon$ is determined by the interlayer adhesion energy for non-bonded interactions, $\sigma$ is the specific distance between two non-bonded beads where the non-bonded potential energy $U_{nb}$ is equal to zero, and $r_c$ is the cut off beyond which the nonbonded effects are zero.

So, in total, there are 5 parameters $(D, \alpha, K_a, K_d, \epsilon)$ that require calibration so as to simulate the mechanical properties of different 2D materials.

The developed CG model is related to the mechanical behavior of different systems that reproduce certain 2D materials and the mechanical constitutive properties of those materials. Therefore, I choose the method of strain energy conservation as the calibration method of the model. In this method, the parameters of the CG potential-field are selected to match certain mechanical properties of the model, including the in-plane Young's modulus, $E$, which is obtained by applying a uniaxial strain and thus determining the stress-strain relationship, the failure strain in two different directions, armchair and zigzag, $\epsilon_{arm}$ and $\epsilon_{zig}$ , the tensile strength, $\sigma_{arm}$ , and $\sigma_{zig}$ as listed in Table 2-1. The in-plane tensile properties can be solely determined by the bond potential. The two parameters which determine the bond potential, namely $D$ and α, can be systematically tuned to reproduce the Young's Modulus, failure strain, and tensile strength based on the expressions below,

$$\epsilon_{arm}(\text{or } \epsilon_{zig}) = \frac{\ln(2)}{\alpha * r_0} \tag{2.6}$$

$$E_{arm}, (\text{or } E_{zig}) = \frac{2 * D * \alpha^2}{{r_0}^2} \tag{2.7}$$

$$\sigma_{arm}(\text{or } \sigma_{zig}) = \frac{D * \alpha}{r_0 * h} * \left(1 - e^{-\alpha * \left((1+\epsilon) * r_0 - r_0\right)}\right) * e^{-\alpha * \left((1+\epsilon) * r_0 - r_0\right)} \tag{2.8}$$

where $h$ is the interlayer distance. First, I determine $D * \alpha^2$ and $\alpha$ by varying Young's modulus and failure strain, respectively, around the target value. Then I calculate tensile strength based on the $D$ and $\alpha$ above. Next, I calculate the difference between current value and target value for Young's modulus, failure strain and tensile strength. I pick out the $D$ and $\alpha$ values with the smallest relative error for the mechanical properties under considerations as listed in supplementary material Table 2-2.

**Table 2-1** Summary of the in-plane mechanical properties of the CG model.

| | **Graphene** | **Borophene** | **BP** | **Silicene** | **$MoS_2$** |
|---|---|---|---|---|---|
| *Young's Modulus* $E_{arm}$ | 965GPa[55] | 1127GP[62] | 33.5GPa[63] | 144GPa [64] | 166GPa[63] |
| *Young's Modulus* $E_{zig}$ | 965GPa [55] | 490GPa [62] | 105.5GPa[63] | 117GPa[64] | 166GPa [63] |
| *Tensile Strength* $\sigma_{arm}$ | 81GPa[55] | 77.363GPa [62] | 4GPa[63] | 11GPa [64] | 18GPa [63] |
| *Tensile Strength* $\sigma_{zig}$ | 64GPa [55] | 30.945GPa [62] | 8GPa[63] | 13.6GPa [64] | 16GPa[63] |
| *Failure Strain* $\epsilon_{arm}$ | 11% [55] | 14% [62] | 23%[63] | 7% [64] | 20% [63] |
| *Failure Strain* $\epsilon_{zig}$ | 15% [55] | 14% [62] | 12%[63] | 14% [64] | 21% [63] |
| *Timestep upper limit* $\Delta t$ | 62.8 fs | 58.38 fs | 106.99 fs | 177.22 fs | 304.58 fs |

**Table 2-2** Parameter of the CG model force-field.

| | **Graphene** | **Borophene** | **BP** | **Silicene** | **$MoS_2$** |
|---|---|---|---|---|---|
| *Bond* | $r_0 = 25Å$[61]<br>$r_{cut} = 30.7Å$[61]<br>$D = 965.6661eV$<br>$\alpha = 0.1216Å^{-1}$ | $r_0 = 25Å$[61]<br>$r_{cut} = 28.5Å$[62]<br>$D_{arm} = 338.08eV$<br>$D_{zig} = 156.04eV$<br>$\alpha_{arm} = 0.1980Å^{-1}$<br>$\alpha_{zig} = 0.1980Å^{-1}$ | $r_0 = 25Å$[61]<br>$r_{cut} = 29.375Å$[65]<br>$D_{arm} = 38.21eV$<br>$D_{zig} = 42.11eV$<br>$\alpha_{arm} = 0.1205Å^{-1}$<br>$\alpha_{zig} = 0.2310Å^{-1}$ | $r_0 = 25Å$[61]<br>$r_{cut} = 27.75Å$[64]<br>$D = 32.11eV$<br>$\alpha = 0.2521Å^{-1}$ | $r_0 = 25Å$[61]<br>$r_{cut} = 30Å$[63]<br>$D = 159.22eV$<br>$\alpha = 0.1386Å^{-1}$ |
| *Angle* | $K_a = 36.6eV$ [61]<br>$\theta_0$ =90° | $K_a = 42.43eV$ [66]<br>$\theta_0$ =90° | $K_a = 10.82eV$ [67]<br>$\theta_0$ =90° | $K_a = 5.48eV$[64]<br>$\theta_0$ =90° | $K_a = 15.78eV$[68]<br>$\theta_0$ =90° |
| *Dihedral* | $K_d = 0.1661eV$ [61] | $K_d = 0.0553eV$ [66] | $K_d = 0.8922eV$[67] | $K_d = 5.3470eV$ [64] | $K_d = 1.5226eV$[69] |
| *Non-bond* | $r_{cut} = 8.67Å$<br>$\epsilon = 20.60eV$[61]<br>$\sigma = 2.89Å$ | $r_{cut} = 10.92Å$<br>$\epsilon = 35.31eV$ [70]<br>$\sigma = 3.64Å$ | $r_{cut} = 11.07Å$<br>$\epsilon = 59.83eV$ [70]<br>$\sigma = 3.69Å$ | $r_{cut} = 11.48Å$<br>$\epsilon = 78.86eV$ [70]<br>$\sigma = 3.83Å$ | $r_{cut} = 15.51Å$<br>$\epsilon = 38.82eV$[71]<br>$\sigma = 5.17Å$[71] |
| *Interlayer distance* | $h = 3.35Å$[55] | $h = 3.23Å$[62] | $h = 5.29Å$[65] | $h = 4.3Å$ [64] | $h = 6.092Å$ [63] |

2.2.3. Model validation

In this work, I perform CGMD simulations by using the massively parallel simulator software--LAMMPS[72]. The timestep $\Delta t$ of CGMD simulations should be carefully selected to allow the lowest vibrational frequency of the bonds to be adequately sampled. When the deformations are relatively small, the difference between harmonic bond potential and Morse bond potential is marginal. Therefore, the frequency of a harmonic oscillator can be shown as $\omega = \sqrt{2k/m}$, where $k$ is the bond stiffness and m is the mass[55]. The criterion widely used in the literature for sufficient sampling is $\Delta t < \frac{T}{10}$, where $T$ is the period of the oscillator[55]. The theoretical upper limit of the timestep that I obtained is $62.8947\ fs$. In order to ensure the stability of my simulations, a time step $10fs$ is chosen for the simulations for graphene hereafter. The time steps $10fs$ is also

applicable for other 2D materials according to the timestep upper limit listed in supplementary material Table SI.

The 2D materials sheet(s) lies on the $xy$-plane, in which armchair direction is along the $x$-axis while zigzag direction is along the $y$-axis. And the $z$-axis is perpendicular to the plane of the sheet. In all of the simulations, non-bonded interactions are only applied between beads that are not explicitly connected by covalent bonding including bond, angle, and dihedral. Simulations of out-of-plane bending of a single sheet and adhesion between two adjacent sheets are performed for the calibration process. Figure A-1 shows the comparison of the stress-strain relationships between the CGMD and AAMD models for a pristine graphene sheet. The size of the graphene sheet for both models is $200\text{nm} \times 200\text{nm}$. It can be seen that the stress-strain curve for the CGMD is in good agreement with that from AAMD. Figure A-2 shows the comparison of the stress-strain curves between the CGMD and AAMD for the octagonal structure. The size of the graphene sheet for both models is $200\text{nm} \times 200\text{nm}$. It can be seen that both AAMD and CGMD simulations show similar patterns, namely J-shaped stress-strain curves. Moreover, the fracture stress predicted from CGMD simulations is very close to that from AAMD simulations. Figure A-3 shows the snapshots from both AAMD and CGMD simulations from the same time series. It can be seen that the conformational changes of the kirigami structure from CGMD simulations are very similar compared with those from AAMD simulations. The ligands are first rotated and aligned along the loading direction, consistent with the low stress feature of the first stage. Subsequently, the ligands are significantly stretched under the external loading direction, consistent with the high stress feature of the second stage. However, it could be seen that, in the first stage of the stress-strain curve, CGMD simulations slightly underestimate the overall stress of the simulations. In addition, the crack initiation estimated from CGMD simulations is slightly larger compared with the AAMD

simulations. Those differences between AAMD and CGMD simulations of Octagon-shaped kirigami structures result from the accuracy loss associated with the coarse mapping of the CGMD model, in which one particle represents a cluster of atoms in a $2.5\ \text{nm} \times 2.5\ \text{nm}$ sheet. Overall, the CGMD model adopted here is reliable and accurate for simulating mechanical responses of 2D kirigami structures. Finally, I performed uniaxial stretching of different material sheets to measure the performance of the different models. The simulation set-up applied in the aforementioned simulations is explained below.

In order to take the measurement of the elastic and fracture properties of the model, I use 2D lattice material sheets with the size $200nm \times 200nm$. Due to the changing of the model's width, the number of the beads the system contained varied from $640$ to $4480$. I applied periodic boundary conditions in the loading direction while free boundary conditions are applied in the lateral directions. The system is minimized at the beginning and then equilibrated in the NPT ensemble at $T = 1\ K$ and zero pressure for $5{,}000$ time steps. After equilibration, the uniaxial tensile test is carried out by a strain-controlled method when strain rate is $10^7\ \text{s}^{-1}$, namely enlarging the simulation box by 0.1 percent every 10000 timesteps and relaxing the model in between two adjacent box enlargement, at a strain rate of $10^7 s^{-1}$. The temperature is controlled at $1K$ in NVT ensemble during the uniaxial deformation, to allow for minimal contributions from thermal noise. For each case, five independent runs with different initial velocity profiles are performed to further reduce effects from thermal noise. Simulations with different numbers of unit cell tiles $(1 \times 1;\ 2 \times 2;\ 3 \times 3)$ are performed to test the effect of box size while corresponding results (details are given in supplementary material Figure A-4) indicates that the influence on stress-strain curves is marginal. Therefore, for simplicity, $1 \times 1$ is used for simulations hereafter. My results are presented with the visualization package OVITO[73].

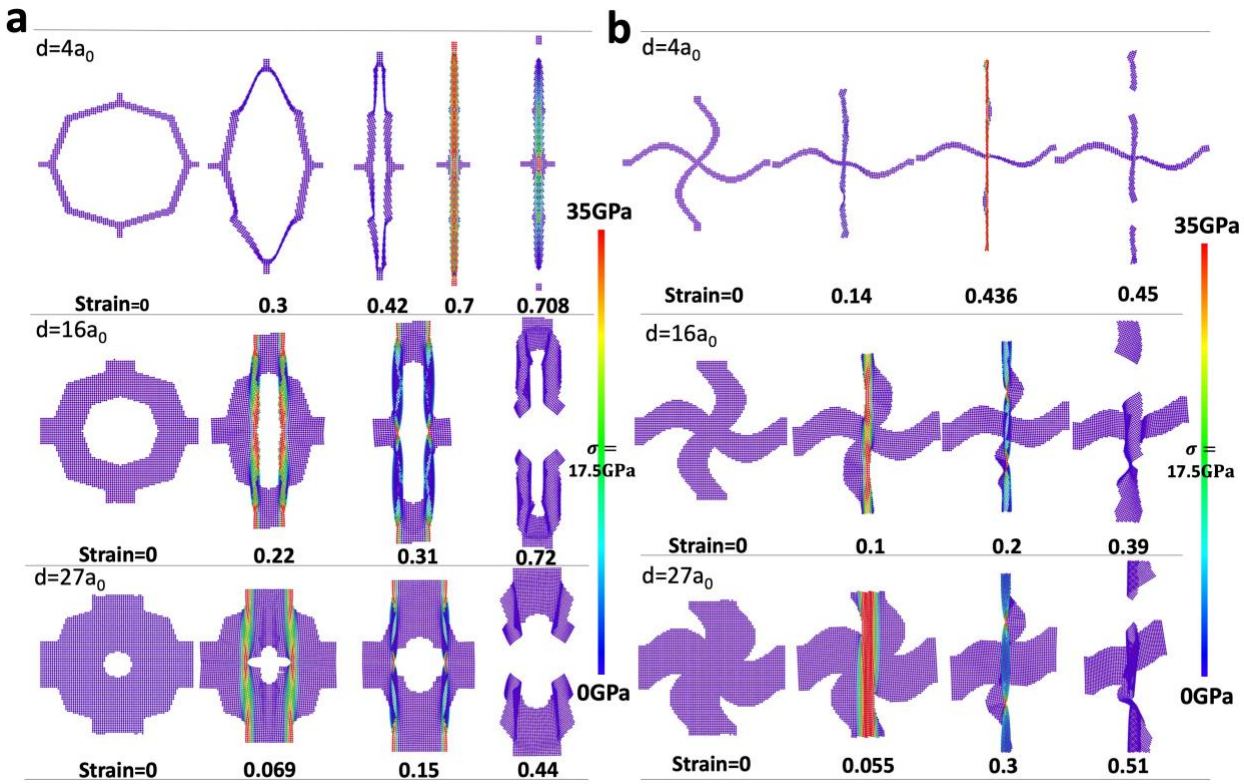


**Figure 2-3** (a) Snapshots of octagonal cell deformation. (b) Snapshots of sinusoidal cell deformation. (I chose four snapshots to show the deformation under tension: the first one is before deformation, the second one is before the deformation hit the tensile strength point, the third one is around tensile strength point, and the last one is after the structure completely break. Snapshots are colored by atomic stress.)

## 2.3. Results and discussion

### 2.3.1. Cell structure effect

#### 2.3.1.1. Structure analysis

There are two classes of the stress-strain relationships for the cells with an inner hole, and they are distinguished according to the degree of change in the slopes of the stress-strain curves. For further explanation, here I choose the stress-strain curve of the octagonal unit cell for illustration (Figure 2-2a). For octagonal cells with a characteristic width between 4 $a_0$ and 18 $a_0$, the slopes of the stress-strain curves change during the stretching process. From 20 $a_0$ to 28 $a_0$, the slopes of stress-strain curves barely change. The above transition from nonlinearity to linearity associated with the

width increase is due to the decreasing rotation ability of the structure components (Figure 2-3a). When the characteristic width is relatively small, the deformation of the model is mainly from the rotation of ligands with minor deformation of the material itself (Figure 3-3a), resulting in marginal stress increase, which can be termed as a free-stress stage. After the ligand aligns along the loading direction due to stretching, stress starts to increase dramatically due to the deformation of the material itself while the elastic modulus gradually becomes a constant. However, as the width of the model increases (Figure 3-3a), the ability of structural rotation is restricted as the structure becomes closer to a pristine sheet of material. Therefore, the 2D material itself is stretched at the very beginning, rather than undergoing structural changes, thus the free-stress stage shortens.

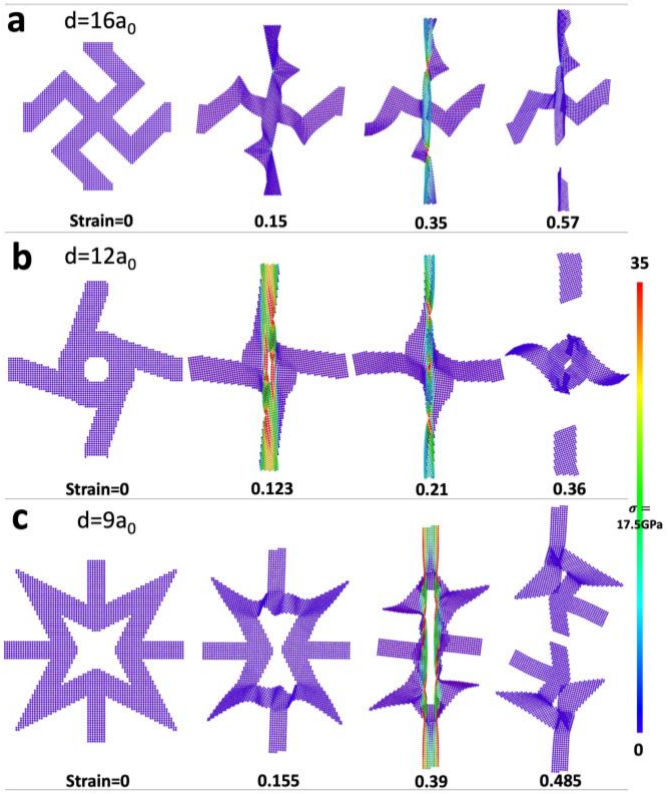


**Figure 2-4 (a**)Snapshot of bent-cross cell deformation. (b) Snapshots of sinusoidal cell deformation. (c)Snapshot of star-shaped cell deformation. (The snapshots are picked out in the same manner as described in Figure 2-3)

The slopes of the stress-strain curves of the cells without an inner hole, such as the sinusoidal and bent-cross unit cells, also show similar behavior to the cells discussed previously. Here I choose the stress-strain curve of the sinusoidal unit cell for illustration (Figure 2-2b). Since there is no hole in these cells (Figure 2-3b, Figure 2-4a and 2-4b), the rotation ability of the structural components is weaker than that observed in the structures with an inner hole, which makes the cells not as stretchable as the cells with an inner hole. It can be easily seen from their stress-strain curves (Figure 2-2), under the same width, the yield strain of the sinusoidal cell is smaller than the octagonal cell. Meanwhile, also due to the structural difference, the material itself is stretched at the very beginning with the no-hole cells (Figure 2-3b, Figure 2-4a and 2-4b), and so the free-stress stage occurs over a much smaller range of strain than for the hole-in cells.

Another interesting phenomenon is the transition of fracture patterns (Figure 2-3). For the cells with an inner hole, when the width is below 8 $a_0$, the model breaks abruptly after reaching the stress peak, indicating a brittle structural failure (Figure 2-3a). In contrast, when the width further increases, the model experiences a jagged stress-strain response after a dramatic stress decrease (Figure 2-2). This fracture pattern change can be attributed to stress localization due to the increase in width. When the width is below 8 $a_0$, it can be seen that the entire cell is under a high-stress status before crack initiation. After crack starts to nuclearize in the bridges (Figure 2-3a), the bonds in that region are broken abruptly, resulting in a brittle failure. In comparison, when the width is larger than 8 $a_0$, the stress localizes at the inner edge of the hole right accompanied by crack initiation and propagation along the central line of the cell through cleaving bonds (Figure 2-3a), resulting in a ductile failure. Therefore, the jagged stress-strain response reflects bond breaking within the structure. No-hole cells also display the jagged-like stress-strain responses due to the bond breaking of the structure. But for this type of structure, the crack initiation of brittle failure

occurs at the same position with the crack initiation of ductile failure, appearing at a turning point of the structure (Figure 2-3b, Figure 2-4) where stress concentrates.

In order to further study the specific fracture patterns of different structures, here I choose the medium-width model to compare their fracture patterns. For the hole-in structure, namely octagonal and star-shaped cells, the model breaks at the turning point of the inner hole (Figure 2-3a and Figure 2-4c), where are the sharp corners located. Sharp corners would be stress concentration sites, with being possible candidates for crack nucleation and deteriorating the strength and toughness of the entire structure. As it can be seen from Figure 2-4c, the shapes of sharp corners are highly distorted due to mechanical extension. Specifically, it can be told from the snapshot when the strain is 0.39 that these sharp corners are in red, indicating high stress concentration. Consequently, the cracks nucleate in these sites, leading to final rupture for star-shaped kirigami as shown in the snapshot when the strain is around 0.485 in Figure 2-4c. In Figure 2-7a and 2-7b, it can be seen that the performance of star-shaped kirigami structures in strength and fracture energy is worse than octagon-shaped and bent-cross kirigami structures with less sharp corners. Overall, sharp corners of star-shaped kirigami would lower the mechanical performance due to stress concentration. For the no-hole structures, bent-cross and sinusoidal cells, the models break at the turning point of the ligand (Figure 2-4a and Figure 2-3b). Although the fan-shaped cell has an inner hole, the hole is not large enough to support similar structural rotation observed in the octagonal and star-shaped cells. During the deformation, crack initiation actually occurs at the connection point between the central circle and the ligand. Therefore, it shows similar behaviors to no-hole cells (Figure 2-4b). Moreover, it can be also seen that, before the out-plane deformation reaches its peak (Supplementary material Figure A-7), the stress does not show a dramatic increase, which provides the existence of free-stress stages. Different cell shows varying

lengths of free-stress stages under the same characteristic width, but they all follow a similar inversely decreasing trend of the free-stress stage as width increases, due to the ability of the structure to hamper rotation. This rotation tunability opens a window to alter the influence of structure on each cell's tensile behavior.

2.3.1.2. Energy analysis

To gain a deep understanding of the mechanical performance of 2D material-based cellular kirigami structures, the potential energy evolution of different types of interactions, such as bond, angle, and dihedral have been analyzed in this section. Figure 2-5a shows the system energy contribution from angle bending (normalized by particle number) versus strain. It can be seen that in the first stage of deformation, the energy change has a minimal contribution from angle deformation. This stage coincides with the free-stress stage in the stress curves, further confirming that in the free-stress stage the deformation is mainly attributed to rigid body motion, rather than material deformation. Moreover, as the width decreases, the peak values of the curves increase, indicating an increased shear deformation of the material which is also in good agreement with the deformation pattern in Figure 2-3a. Figure 2-5b shows the normalized energy contribution from bond stretching versus strain. Interestingly, the peak value of bond energy undergoes a decrease followed by an increase as the width increases. When width increases from $4a_0$ to $18a_0$, the peak bond energy decreases due to decreased rotation ability of the ligands. As can be seen in Figure 2-3a, right before fracture, all the ligands are fully stretched along the loading direction, enabling a larger fracture strain than the bending-dominated samples with larger ligand width. The small width characteristics render a low bending stiffness of the 2D cells in this study, leading to an increased out-of-plane deformation with the stress concentration within the material also being lower. Therefore, a relatively greater amount of energy comes from bond stretching. As width

increases, the bending stiffness of ligands increases, and the rotation ability decreases with the stress concentration being high. Therefore, when the crack initiates, cells with a thicker width achieve a lower average bond energy compared with models with thinner ligands width. However, when the width increases beyond 18 $a_0$, the average bond energy increases due to the increasing connectivity in materials. It can be seen in Figure 2-3a, the ligands barely rotate while the material is under a more uniform stress distribution with stress concentration around the hole compared with models with the width equal to 18 $a_0$ as shown in Figure 2-3b. Figure 2-5c shows the average dihedral energy change versus strain. It can be seen that, regardless of width change, the dihedral energy would increase to the same level. In addition, the dihedral energy will not increase dramatically until the structure approaches fracture. Overall, the dihedral energy contribution is two orders of magnitude smaller than the in-plane strain energy, i.e. bond and angle energy. Figure 2-5d shows the total potential energy change versus strain. It can be seen that the average potential change peak undergoes a marginal change due to the competition between stretching and bending deformation. However, as the width decreases further, average potential energy increases dramatically as both bond and angle energy increase intensively. Figure 2-6 also shows the average strain energy of sinusoidal cell versus strain. It can be seen that, despite different geometrical designs, the maximum peak values for bond and angle energy for different widths are very close to each other, which indicate that the fracture of 2D materials based kirigami cell structures are ultimately controlled by materials. The comparison between potential energy changes of sinusoidal and octagonal cells show that the geometrical designs can make a difference for mechanical performance, especially for fracture strain.

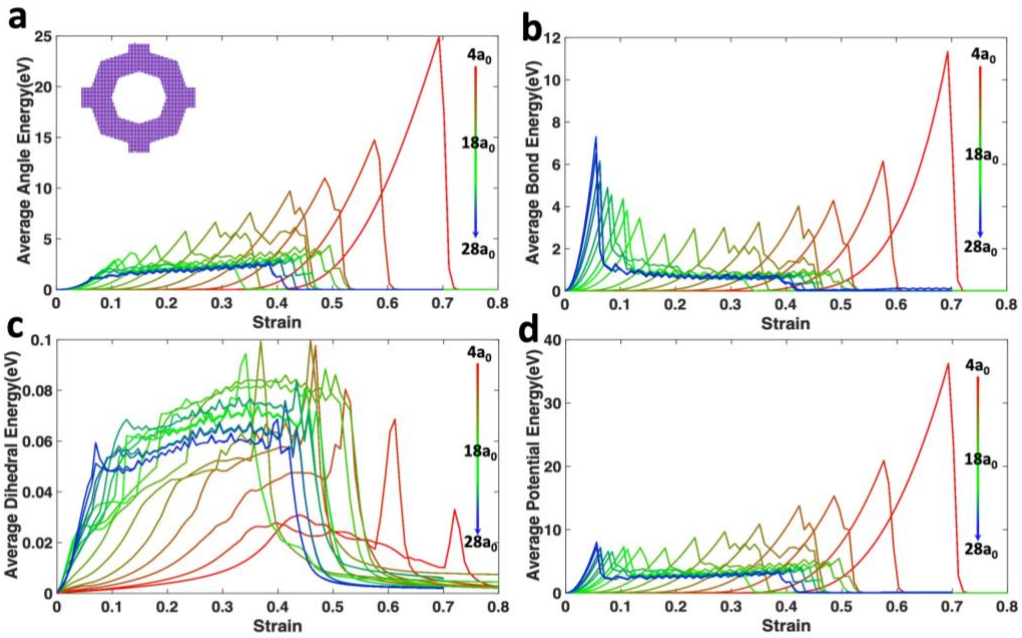


**Figure 2-5** Energy evolution of octagonal cell based on graphene. (a) Angle Energy (b) Bond Energy (c) Dihedral Energy (d) Summation of Potential Energy (Note that the energy changes here are all normalized by the number of particles).

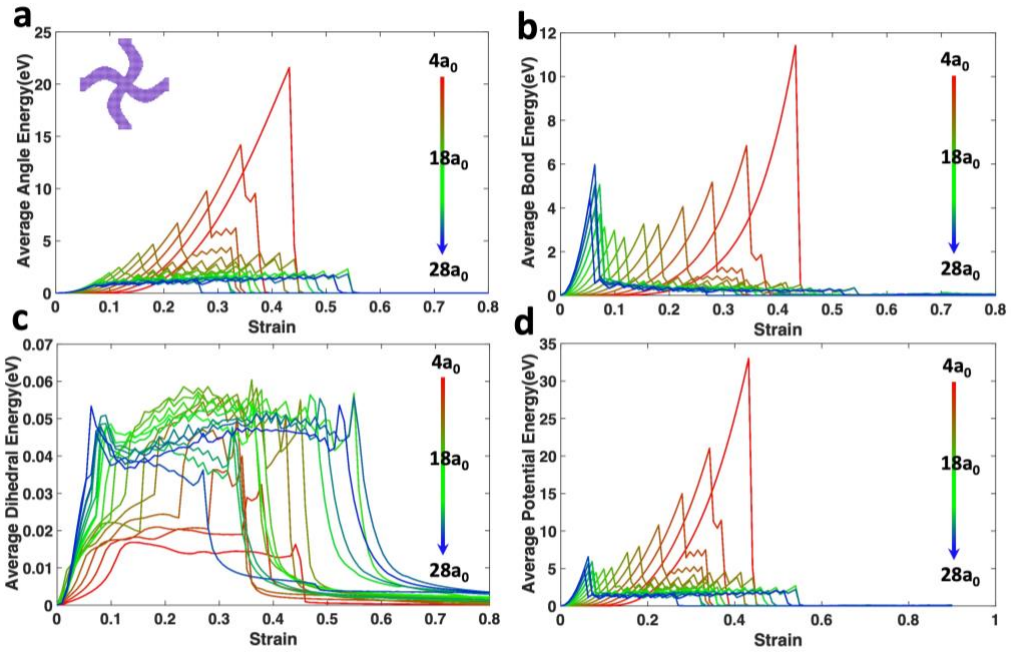


**Figure 2-6** Energy evolution of sinusoidal cell based on graphene. (a) Angle Energy (b) Bond Energy (c) Dihedral Energy (d) Summation of Potential Energy (Note that the energy changes here are all normalized by the number of particles)

2.3.1.3. Property analyses

Here, I analyzed their mechanical properties versus "density", which is an indicator of porosity. For a $200\text{nm} \times 200\text{nm}$ sheet, I define the number of particles without pattern cut as $N_{sum}$, equal to 6400 in my case. For different cut patterns, I define the number of particles deleted from the pristine sheet as $N_{del}$. Similarly, I define the number of particles remaining as $N_{rem}$ for different patterns as shown in Figure 2-1. The density of different kirigami structures, denoted as $\rho$, can be calculated with the expression below,

$$\rho = \frac{N_{rem}}{N_{sum}} * \rho_{mat} \tag{2.9}$$

where $\rho_{mat}$ is the density of different 2D materials without any cut. It is straightforward to tell that, when the width of ligands increases, the density $\rho$ approaches to the material density $\rho_{mat}$. The hole-in structures show a good performance on ductility, namely free-stress strain and yield strain due to the inner hole (Figure 2-7). In addition, the octagonal cell outperforms all other tested cells by the metrics of tensile strength and fracture energy due to its wider density range. The main structural difference between the star-shaped and octagonal cells is the shape of their inner hole. The octagonal cell has a convex hole while the star-shaped cell's interior hole is concave. Therefore, the star-shaped cell shows the extraordinary performance on free-stress strain and yield strain due to the concave shape of the inner hole, which allows for greater deformation due to the structure change. However, the octagonal cell shows a greater change in fracture energy, while the fracture energy of the star-shaped cell barely changes as the density increases due to the structural difference between the hole of these two cells. Specifically, sharp corners of star-shaped cell inhibit the rotation of ligands and induce high stress localization, resulting in relatively poor ductility and low fracture energy.

For no-hole structures, the bent-cross one shows the weakest performance on tensile strength, while sinusoidal cell displays superior properties (Figure 2-7). This can be mainly attributed to the difference between their structures, with the bent-cross cell having sharp structural angles, allowing for higher stress concentration and thus earlier material failure. However, the bent-cross cell shows a greater free-stress strain region at small strain, allowing for improved performance for certain applications. Overall, the mechanical performance of the cells with an inner hole is superior in every aspect. Even though the fan-shaped cell shows similar behavior with no-hole structures, the tensile strength still slightly outperforms the other two cells due to the inner hole brings the fan shaped cell a better connection between the ligands (Figure 2-4b). However, the fan-shaped cell shows the weakest performance on fracture energy, due to the weaker rotation ability and higher stress concentration factor. Specifically, the high stress concentration factor results from a mismatch between the loading axis and the direction axis of ligands.

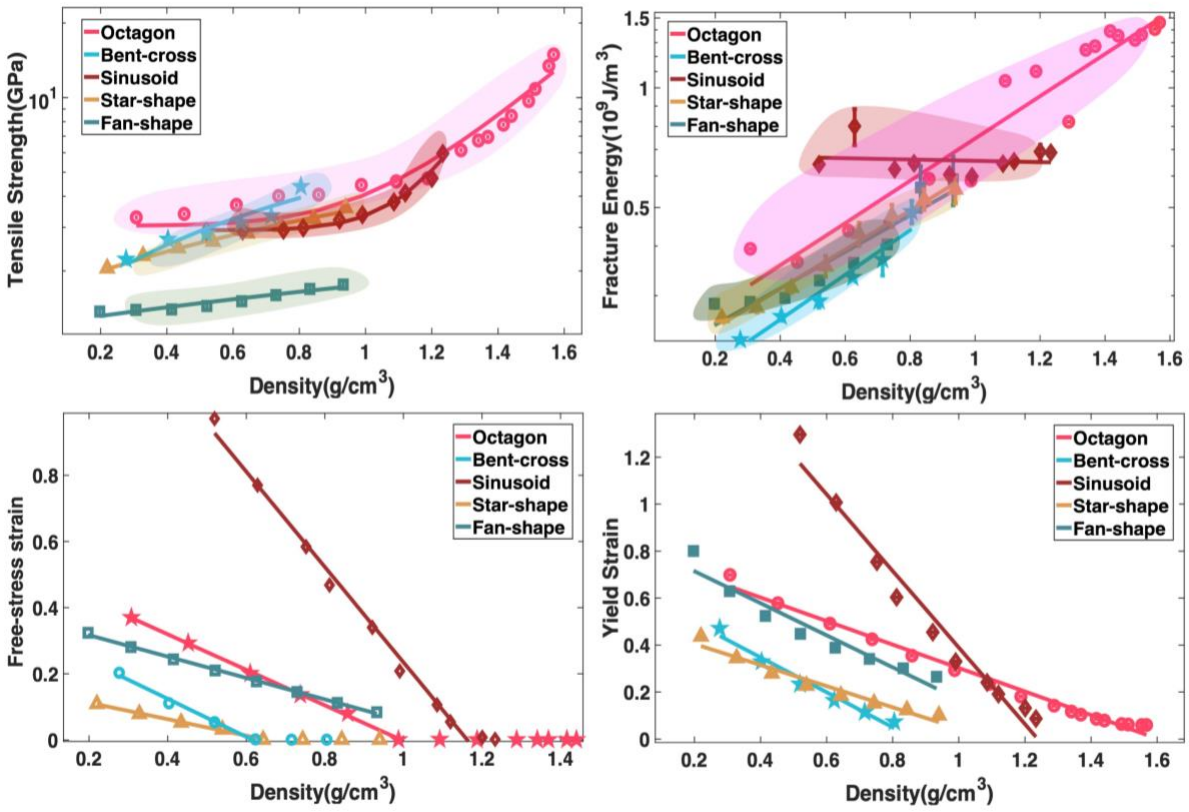


**Figure 2-7** Graphene-based mechanical properties changes of five structures (a) Tensile Strength (b) Fracture Energy (c) Free-stress Strain (d) Yield Strain. (a and b are semi-log plots.)

With mechanical properties being fitted with analytical expressions, their performance of these 2D materials based kirigami cells can be compared with other porous materials, which can be described by polynomial scaling laws [74-78]. For 3D porous materials, the order of polynomial scaling laws varies from 1 [74] to 3 [78] based on the deformation pattern. For a stretch-dominated structure, the ultimate strength scales linearly with density [74]. However, for a bending-dominated structure, the mechanical performance would follow a polynomial scaling law with a higher order [78]. For tensile strength in Figure 2-7a, I use a fifth order polynomial function, the order of which is higher compared with previous studies. The high order of scaling laws can be attributed to the competing two deformation patterns, namely stretching and bending. For instance, octagonal cell with a characteristic width smaller than 18 $a_0$ follows a stretch-dominated deformation pattern as

shown in Figure 2-3a, resulting in a linear and moderate increase in ultimate strength. In contrast, as the width increases, bending starts to dominate while the ultimate strength increases nonlinearly and dramatically.

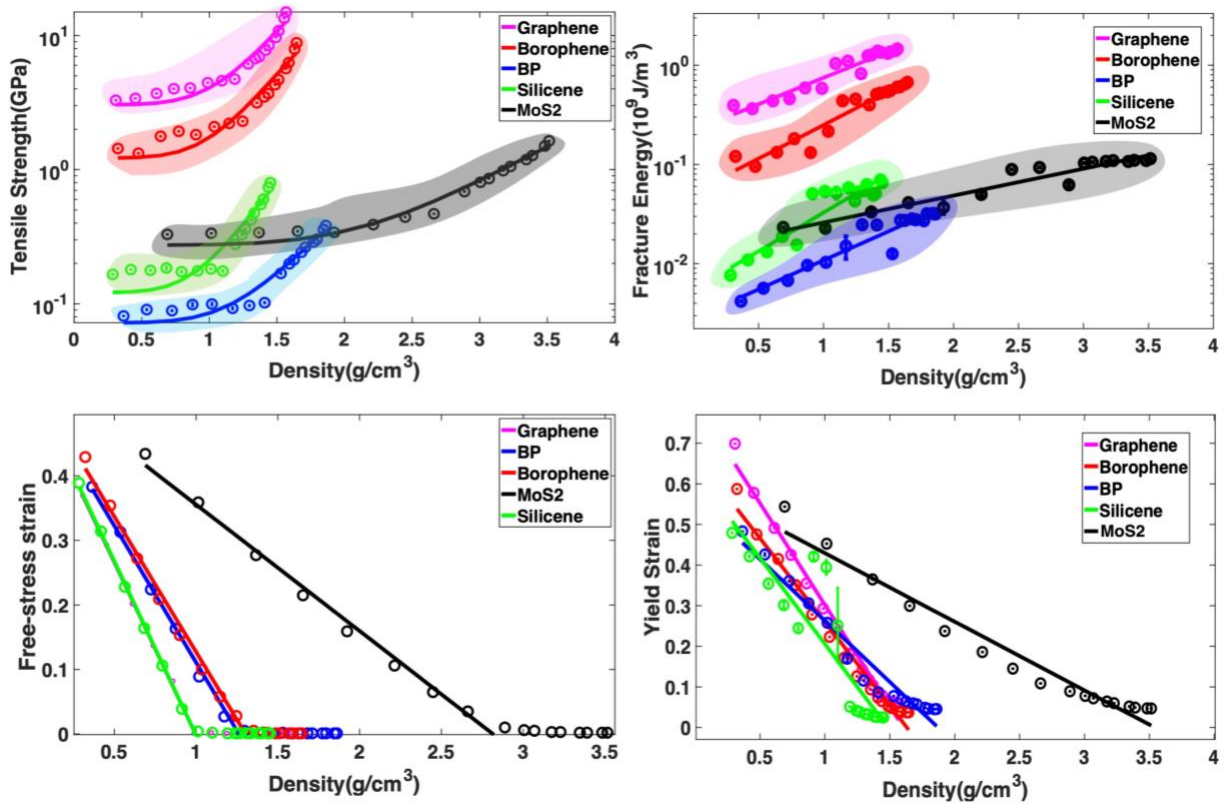


**Figure 2-8** Mechanical properties changes of octagonal cells based on five 2D materials. (a) Tensile Strength (b) Fracture Energy (c) Free-stress Strain (d) Yield Strain. (a and b are semi-log plots)

2.3.2. Material effects

Five different 2D materials are chosen to investigate the material effect on mechanical performance, namely graphene, borophene, black phosphorus, silicene, and $MoS_2$(Figure 2-8). For the sake of simplicity without loss of generality, I choose the octagonal cell as a typical example to study them (details are given in supplementary material Figure A-6). Here I use exponential functions to fit the fracture energy, and polynomial function to fit the tensile strength. The free-

stress strain and yield strain are fitted by linear function. Results indicate that although they all show similar behaviors, graphene outperforms the other 2D materials regarding tensile strength and fracture energy due to the outstanding mechanical properties of material itself. But for free-stress strain and yield strain, the difference between materials shows limited effect on the results, demonstrating that the structural geometry is a dominating factor for these properties. Note that MoS2 shows a great span of density compared with the other materials due to its much higher density for pristine structures. Based on my calculation, the density for MoS2 is around 5.09 g/cm$^3$, much higher than the other materials (borophene 2.38g/cm$^3$, phosphorene 2.70 g/cm$^3$, graphene 2.27g/cm$^3$, silicene 2.10 g/cm$^3$). The cutting pattern and the width range of ligands are the same, however, the higher density of MoS2 enables a broader range of density for MoS2-based kirigami structures in Figure 2-8. Overall, the structure dominates the property trends, while the chosen materials determine the exact values.

Ultimate strength and fracture toughness of the 2D materials based kirigami cells displayed here are exceptional compared with other materials in the literature [77]. The density of structures here ranges from ~400 to ~4000 kg/m$^3$, falling in the range of polymers, ceramics and glasses [77]. However, the ultimate strength varies from 0.1 to 10 GPa, which is among the top level of both synthetic and natural materials in this density range. The fracture energy, namely fracture toughness, is in the range of 10 to 1,000 $MJ/m^3$, ranks in the top class of materials for this density range. For instance, a previous study has reported a porous material design made of silicon in the similar range, while the toughness is from 300 to 600 $MJ/m^3$ [75]. In Figure A-8, the normalized mechanical properties have been plotted as a function of density. It can be seen that, for the normalized strength and fracture energy, the magnitudes are all below 1, meaning that the performance of 2D material kirigami pales in comparison to their base material. However, the

normalized yield strain for most kirigami structures is above 1, meaning that the kirigami structures outperform their base materials in deformability. The deterioration of strength and fracture energy for kirigami structures originates from the stress concentration at the sharp cuts as shown in Figure 2-3 and Figure 2-4. However, the strengthening of yield strain for these kirigami structures can be attributed to the outstanding deformability of the ligands. Overall, the kirigami structures designed here shows great enhancement in terms of deformability. Moreover, as discussed before, the J-shaped stress-strain responses under external forces as shown in Figure 2-2 are very similar to those of biomaterials, enabling them a good compatibility in medical applications. Overall, the material performance of the structures here are outstanding while the polynomial scaling law can provide guidelines for design of kirigami based on 2D materials.

### 2.4. Conclusion

In the present paper, the underlying research of enhancing the mechanical properties of 2D materials by using different kirigami structures, and the effects of structure and unit cell parameters have been investigated. With the developed CG model that can be readily extended to other materials, I also presented the relationship between mechanical performance with different materials. Results indicate that there are two stress-strain behavior patterns associated with density, J-shape non-linear and linear elasticity. The transition of those two stress-strain patterns results from the variance of rotation ability of ligands due to the variance of width. Moreover, results indicate that structures with the inner hole show a good performance on ductility, namely free-stress strain and yield strain. The effect of material on mechanical performance have also been investigated, in which graphene, silicene, phosphorene, borophene, and molybdenum disulfide ($MoS_2$) are chosen. Graphene outperforms the other 2D materials regarding tensile strength and

fracture energy due to the outstanding mechanical properties of material itself. Overall, research findings here deepen our understanding the relations between mechanical performance and structure pattern as well as component material properties for 2D material based cellular kirigami structures. Therefore, my results could provide useful guidelines for designing and fabricating metamaterials with exceptional mechanical performance.

# CHAPTER3 DESIGN ARCHITECTURED GRAPHENE KIRIGAMI USING MACHINE LEARNING

## 3.1 Introduction

The rapid development of science and technology begets higher and higher requirements for the performance of materials, especially in aerospace instruments, precision medical equipment, high-tech electronic products, and other fields which generally require materials to have good conductivity, light weight, and high strength performance simultaneously. The lack of a suitable material to meet multiple needs at the same time has always restricted the development of products in these high-tech fields. In 2004, physicists Andre Geim and Konstantin Novoselov[79] of the University of Manchester in the United Kingdom successfully isolated graphene from graphite and verified that it has a variety of excellent performance properties through multiple studies. The emergence of this new material has shown its great potential in various fields as soon as it was discovered. This immediately attracted widespread attention in materials science, physics, and other fields, especially with the continuous deepening of its performance research. Although graphene has a variety of excellent properties, it is a brittle material, and its relatively small failure strain has greatly limited its application in elastic and flexible electronic devices and aspects. The failure strain obtained by numerical simulation is only about 0.2, and is even smaller when tested by experiment[79]. This limitation greatly hinders applications for graphene. Cornell University physicist Paul McEuen[20] pointed out that ordinary paper cannot be stretched, but if you introduce some cuts in it, it can; his team introduced this concept, called “kirigami”, to graphene to allow for significant improvement in tensile tests. Graphene kirigami can be considered to open another door

for graphene applications. The Paul McEuen[20] research group of Cornell University first successfully prepared monolayer graphene kirigami through experimental methods, and conducted tensile simulation tests on them, and demonstrated that graphene kirigami has strong deformability. Molecular dynamics simulations showed that the yield and fracture strain of monolayer two-dimensional graphene kirigami can reach 3 times that of perfect graphene, which fully demonstrated the broad application prospects of graphene kirigami in flexible electronic devices and composite materials[80]. However, how to adjust the mechanical properties of graphene kirigami to meet work needs is still an open question.

Architectured 2D kirigami structures show many unique mechanical properties, such as ultrahigh specific failure strain, tensile strength, and toughness, as well as a potential for a negative Poisson's ratio[29]. Beyond that, these unique mechanical properties are governed by the structure, rather than material. Their independence to composition material brings tremendous potential towards application in flexible electronics, mechanically controllable thermal structures, and structurally tunable optical and phononic devices[81]. It is expected that the combination of reasonably designed architectured 2D kirigami structure using monolayer graphene sheets can not only improve the mechanical properties of graphene, but also allow them to be adjustable for different needs. However, most existing architectured structures, usually called mechanical metamaterials, are periodically arranged with a repeating unit cell. This type of arrangement design limits the diversity of the mechanical performance of the composed material. By increasing unit cell diversity and assembling heterogeneous architectured structure unit cells to a modal grid has made several mechanical metamaterials achieve programmable mechanical properties. This method allows the network connection of grid architectured structure to be modified by changing the arrangement order of the unit cells. However, the combination of a simple grid architectured

structure can be massive depends on how many structure unit cells are provided. Therefore, the simulation progress of exploring all the possibilities of these grid architectured structures is as good as impossible to fully complete due to computational resource limitations.

Machine learning (ML) methods show huge potential to screen across a huge design space[81]. ML has been used to study and design materials with low thermal conductivity, such as porous graphene. ML has also been applied to design functional materials and structures, such as graphene kirigami with high yield strain[81]. Specifically, a backpropagation (BP) neural network is a multi-layer feedforward network and its learning algorithm is an error back propagation algorithm. BP neural network is currently one of the most mature and widely used artificial neural network models. Because of its simple structure, strong operability, and good self-learning ability, it is widely used in automatic control, pattern recognition, image recognition, signal processing, function fitting, system simulation, and other disciplines and fields. BP neural network can learn and store a plethora of mapping relationships between input and output without revealing and describing a mathematical equation of the mapping relationship before learning. This advantage is more obvious when the input of the network is enormous number of different arrangements of the grid architectured structure, which does not translate well to traditional equation setups.

Here, to thoroughly study how the arrangement of the grid architectured structure directs the mechanical properties of graphene kirigami molecular dynamics (MD) simulations, I use a BP neural network to approximate the tensile strength. To formulate this problem methodically, then setup the architectured graphene kirigami as a 3x3 grid sheet, I designed five different 4-node architectured structures to fit in the grid and perfectly connect to each other. The probability of occurrence for architectured structure unit cell in each grid region will be completely independent,

as shown schematically in Figure 3-1. I then applied the BP neural network for inverse design, where the goal is to maximize the tensile strength of the architectured graphene kirigami. By this inverse design method, my model is able to show the potential of finding the ideal solution by only screening over 2300 cases out of the full design space of 1,953,125. The findings can provide general guidelines to design an architectured graphene kirigami without any prior knowledge of the fundamental physics, which is of great importance when only experimental data are available, and an accurate physical model is unknown.

## 3.2 Method and Validation

### 3.2.1 Designed structures

I introduce and set the focal investigation on five distinct four-node architectured structures with rationally designed architectures. From the geometric parameters shown in Figure 3-1, $d$ is the width of the structural ligands, which is fixed as $10\ a_0$ ; $L$ is the length of the bridges, which is fixed as $0.5\ a_0$ due to the limitation of the structural integrities. The base length unit termed $a_0$ is equal to 2.5 nm. The size of these architectured structure unit cells are $200\text{nm} \times 200\text{nm}$. Then I randomly generate the 3x3 grid architectured graphene kirigami based on these five structures (Figure 3-1). Therefore, the final size of the models that I run by MD simulation is $600\text{nm} \times 600\text{nm}$. All the models are designed using my in-house code written in MATLAB before being exported to LAMMPS for simulation (further details below).

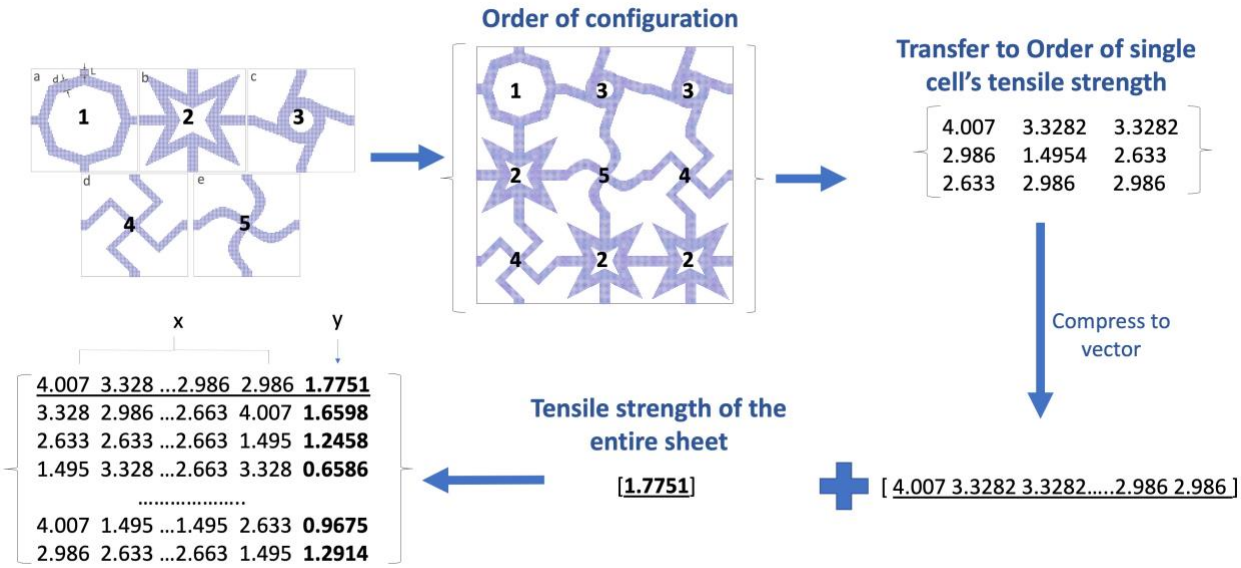


**Figure 3-1** Structure of input dataset.

3.2.2 CGMD simulation

Molecular dynamics uses force fields to calculate the potential energy of molecular systems. Different force fields use different potential energy functions. In terms of computing speed, the all-atom molecular simulation (AAMD) is much slower than the simplified coarse-grained molecular simulation (CGMD) due to the limitation of current computer performance. CGMD is a more simplified force field model. It considers a group of atoms as a unit, thereby greatly reducing the amount of calculations, so it is often used to process functional material systems. Due to the lack of details for molecular structure such as atoms and atomic bonds, the coarse-grained model has a different force field potential from the conventional atomistic molecular force field. Here, I develop a generic coarse-grained potential to simulate large-scale graphene. As opposed to common graphene coarse-grained models such as the Martini force field model which has hexagonal symmetry, my square coarse-grained lattice is a simple but generic model which can be tuned to well capture the mechanical anisotropy in not only graphene, but also other 2D materials.

The good transability of my coarse-grained model makes it easy to be used for similar research and further studies with other materials and structures. Specifically, I use a Morse potential for bonded interactions, a harmonic spring potential for 3-body (angle) interactions, a cosine potential for 4-body (dihedral) interactions, and a Lennard-Jones potential for non-bonded interaction. In total, I have 5 parameters ($D, \alpha, K_a, K_d, \epsilon$) that can be adjusted to make my CG model match the chosen mechanical properties of graphene, which are the in-plane Young's modulus, the failure strain, and the tensile strength in the two in-plane different directions, armchair and zigzag. Detail can be found in the previous chapter.

### 3.2.3 BP neural network

The BP neural network is a multi-layer feedforward network trained by the backpropagation algorithm, referred to as the BP algorithm. It uses the steepest descent method to obtain information that continuously adjusts the weights and thresholds of each connection through backpropagation of the output error, and finally minimizes the mean square error of the neural network to meet the desired requirements. The BP neural network model is a three-layer network, and its topological structure can be divided into the input layer, output layer, and hidden layer. Each layer is composed of many simple neurons that can perform parallel operations. Since the BP neural network is a feed-forward network, it has the characteristics of a feed-forward network, which means all neurons between two adjacent layers are all connected to each other, but neurons in the same layer are not connected.

The fundamental principle of the BP neural network is to pass an input vector through a series of transformations in the hidden layer, and then obtain an output vector, so as to get a mapping relationship between input data and output data[82]. The BP algorithm consists of two parts: forward

propagation and back propagation. The forward propagation of input information and the backward propagation of output errors constitute the information loop of the BP network. Specifically, in the forward propagation process, the input information is transmitted from the input layer to the output layer after being processed by the hidden layer unit[82]. The state of neurons in each layer only affects the state of neurons in the next layer. If the desired output cannot be obtained in the output layer, it will switch to back propagation, that is, return the error along the connection path, and modify the connection weight between the neurons in each layer to minimize the error[82]. Therefore, the BP network has a symmetric network structure, and each processing unit at the output basically has the same activation function.

I used the BP neural network designed by TensorFlow in R. I use the mechanical property of each structure to code the arrangement of the grid architectured structure, which give me 9 features as predictor variables and using the tensile strength of the 3x3 grid architectured structures as the target variable. Specifically, these 9 features are the tensile strength of the single architectural structure in each cell (Figure 3-2). I applied four hidden layers with 40, 20, 10, and 5 neurons included for each of the layers, and the final output layer was used to evaluate the outcome, as shown in Figure 3-2. I added a rectified linear unit (ReLU) function as the activation function after each hidden layer. As a regression problem, the ReLU function will not appear at the final layer. I used 2,483 data sets in total for the learning process; 80% data was used for training and 20% for validation. I used mean square error as the loss function, which is shown below:

$$RMSE = \sqrt{\sum_{i=1}^{n_t} \frac{\left(y_t^i - y_p^i\right)^2}{n_t}} \tag{3.1}$$

Here, $n_t$ is the number of training data, and $y_t^i$ and $y_p^i$ are the true mechanical properties obtained from previous discrete computational models and the predicted mechanical properties by the FNN model, respectively. By optimizing the number of layers and width of the layers, I minimized the root mean square error (RMSE) between the predictions and targets with the RMSprop optimizer, the math equations used in the RMSprop optimizer are show below:

$$E[g^2]_t = \beta E[g^2]_{t-1} + (1-\beta)\left(\frac{\delta C}{\delta w}\right)^2 \tag{3.2}$$

$$w_t = w_{t-1} - \frac{\eta}{\sqrt{E[g^2]_t}}\frac{\delta C}{\delta w} \tag{3.3}$$

where $E[g^2]_t$ represents the moving average of squared gradients. $\frac{\delta C}{\delta w}$ is the gradient of the cost function with respect to the weight. n is the learning rate[83]. $\beta$ is the moving average parameter. I retained the default values for these parameters at my model, where the learning rate *n* is 0.001, and $\beta$ *is* 0.9, respectively.

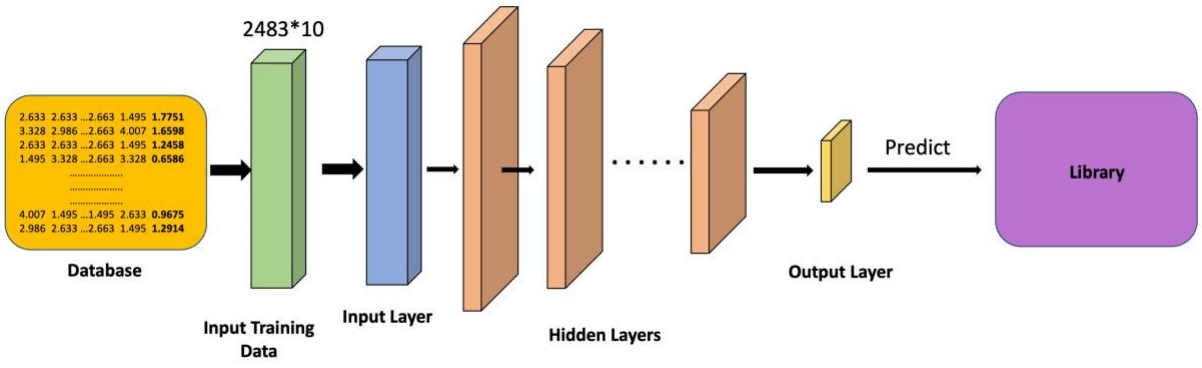


**Figure 3-2** Overview of the method to train a grid architectured graphene kirigami using machine learning model.

## 3.3 Results

### 3.3.1 Mechanical performance of grid architectured graphene kirigami

In the current paper, I have proposed five cellular cutting different patterns for graphene kirigami as shown in Figure 3-1, namely octagon, fan, bent-cross, sinusoid, and star. Special combinations of cellular cutting patterns, namely those with homogeneous unit cell patterns for all $3 \times 3$ cells, are important benchmarks for understanding the structure-property relationship in graphene kirigami. Figure 3-3 shows the stress-strain curves of graphene kirigami with homogeneous cutting patterns. As it can be seen, graphene kirigami unit cell patterns are markedly different in terms of Young's modulus, yield strain, and tensile strength. Despite the significant differences in mechanical performance, all tested graphene kirigami shares the "J-shape" stress-strain responses under uniaxial tension as shown in Figure 3-3. The stress-strain responses can be roughly divided into two stages. In the first stage, the stress increases slowly with the increase of strain. During this stage, the deformation is mostly from rigid body motion of the ligands of the cutting patterns, which induces minor deformation of the material itself and thus achieves low stress. In the second stage, the stress increases intensively associated with the increase of strain. In this stage, the stress increases linearly with the strain while the deformation of the kirigami mainly comes from deformation of the material. Therefore, due to the linear elasticity of graphene, the graphene kirigami also shows linear elasticity in the second stage. At the end of the second stage, graphene kirigami experiences a huge stress drop due to tensile fracture. The ultimate tensile strength of "Octagon" is highest ($4.5\ GPa$) while that of "Bent-cross" is lowest ($1.4\ GPa$). The highest fracture strain is $0.45$ ("Bent-cross") while the lowest one is $0.18$ ("Fan"). Interestingly, some patterns ("Fan") are stiff, strong, and brittle, while some patterns ("Bent-cross") are soft, weak, and ductile. Therefore, through combinations of different cutting patterns, it is possible to design graphene kirigami with tunable mechanical performance.

Figure 3-4 shows the snapshots of two grid graphene kirigami samples, “Octagon” and “Bent-cross”, under uniaxial tension. As shown in Figure 3-3, the yield strain of “Octagon” is very close to that of “Bent-cross”, in the top tier of all the cutting patterns. However, the tensile strength of “Octagon” is much higher than that of “Bent-cross”. The above phenomena can be well explained by Figure 3-4. The good ability of rotation of the ligands in both “Octagon” and “Bent-cross” enables good ductility. It can be seen in Figure 3-4a that when the strain is 0.38 and 0.43, high stress indicated by the color red spreads throughout the model, meaning that the stress distribution is relatively uniform in “Octagon”. In contrast, for “Bent-cross”, only the ligands along the loading direction withstand high stress. Therefore, the percentage of materials used to resist high stress for “Bent-cross” is much lower than that of “Octagon”, resulting in the lower tensile strength.

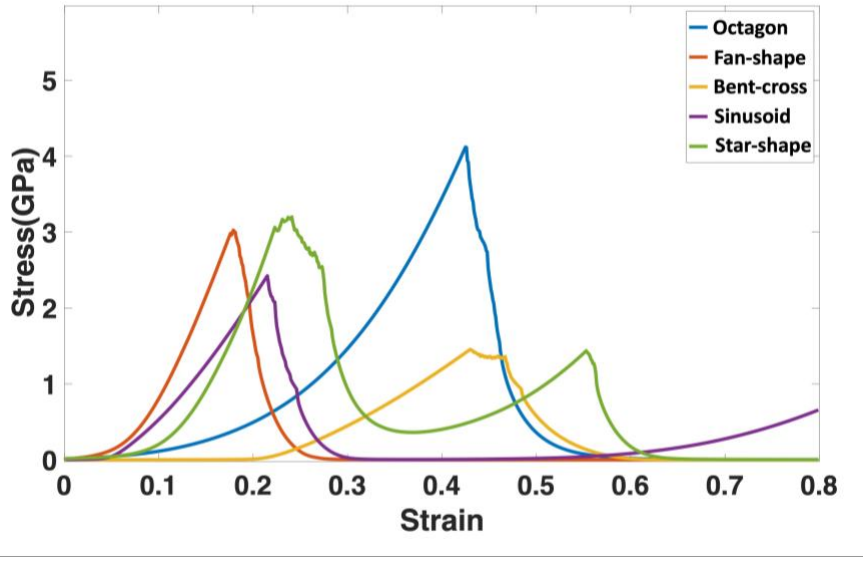


**Figure 3-3** Stress-strain curve of a 3x3 homogeneous grid architectured graphene kirigami based on five different architectured structures.

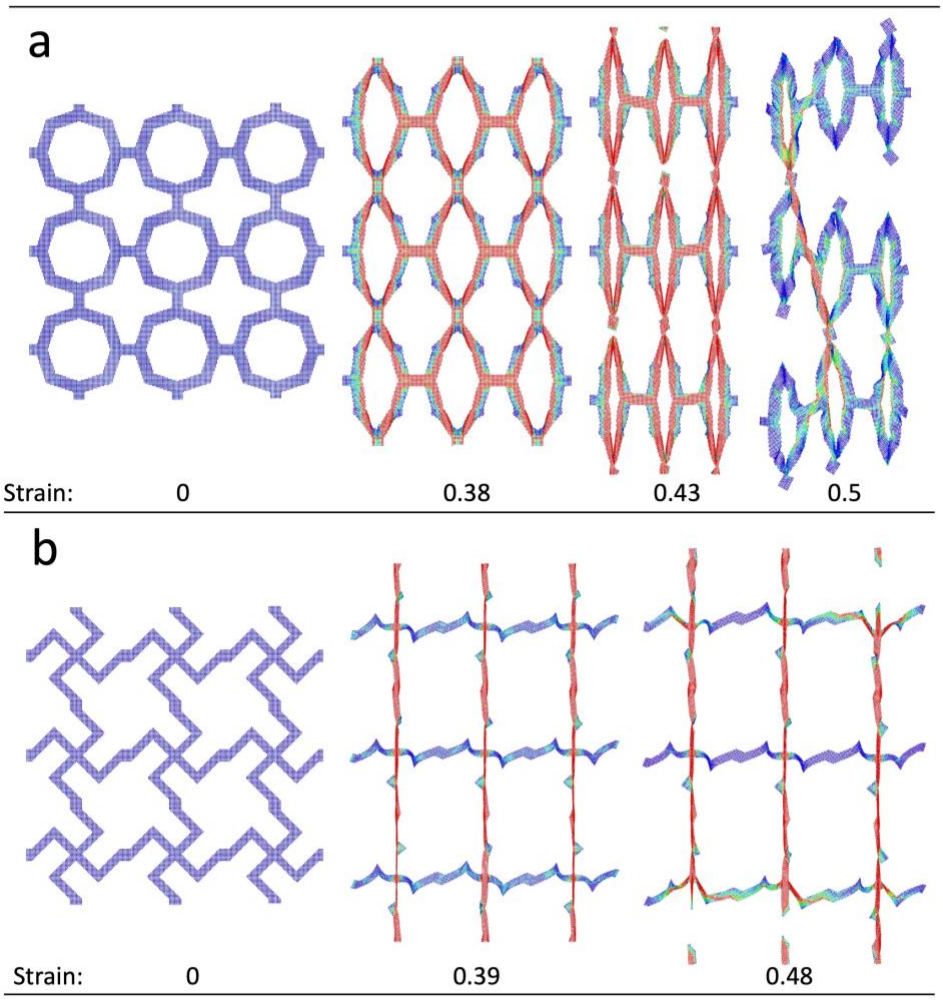


**Figure 3-4** (a) Snapshots of octagonal homogeneous grid architectured graphene kirigami under uniaxial tension. (b) Snapshots of bent-cross homogeneous grid architectured graphene kirigami under uniaxial tension.

3.3.2 Structure-property relationship by machine learning

In the section above, I have analyzed the stress-strain responses of graphene kirigami with homogeneous cutting patterns. To better understand structure-property relationship of graphene kirigami, heterogeneous cutting patterns are introduced in this section for graphene kirigami. Figure 3-5 shows stress-strain curves of graphene kirigami with heterogeneous cutting patterns during uniaxial tension. It can be seen that in Figure 3-5a, the stress-strain curve of "Mix 1" is very close to that of "Sinusoid" because "Sinusoid" patterns are prevalent (5 out of 9) in "Mix 1". Interestingly, although patterns with high strength ("Octagon") are included, "Mix 1" is slightly

weakened instead of enhanced in terms of strength when compared with “Sinusoid”. Note that, although the strength of “Octagon” is much higher than that of “Sinusoid”, the stiffness of “Octagon” is much lower than that of “Sinusoid”. Therefore, “Octagon” cannot enhance the strength because “Mix 1” experiences tensile before “Octagon” reaches its ultimate strength as shown in Figure 3-6a. Figure 3-5b shows the stress-strain curve of “Mix 2”, indicating the intermediate mechanical performance. Figure 3-6 shows the snapshots of “Mix 1” and “Mix 2” under uniaxial tension. Note that the tensile fracture of “Mix 1” initiates in the “Sinusoid” pattern while that of “Mix 2” initiates in the “Fan” pattern, indicating that the yield strain is mainly controlled by the one with lowest yield strain.

Subsequently, I have conducted machine learning simulations to predict the structure-property relationship for graphene kirigami. Three thousand samples with different combinations of cutting patterns are simulated to determine their mechanical performance. An additional six thousand datasets are obtained through the geometrical symmetry of the sample. Figure 3-7 a-b shows the comparison between labels and predictions for tensile strength. The $R^2$ values for “Train” and “Test” are 0.45 and 0.43, respectively. Figure 3-7(c-d) shows the loss and absolute error for the program versus number of epochs, in which both variables drops intensively at the beginning and reaches a plateau by the end. Therefore, the machine learning algorithm reaches a final answer for the problem. The low accuracy of the prediction may come from the incomplete information from the input. Only the tensile strength of the $3 \times 3$ cellular cutting patterns are given for predicting the ultimate strength of the kirigami. However, as discussed before, the tensile strength of graphene kirigami is not only related to the tensile strength of each cellular cutting patterns but also related to the evolving stiffness and strain of those patterns. Therefore, it is necessary to find a way to

include the evolving stiffness of cellular cutting patterns in the input to predict the overall tensile strength of graphene kirigami.

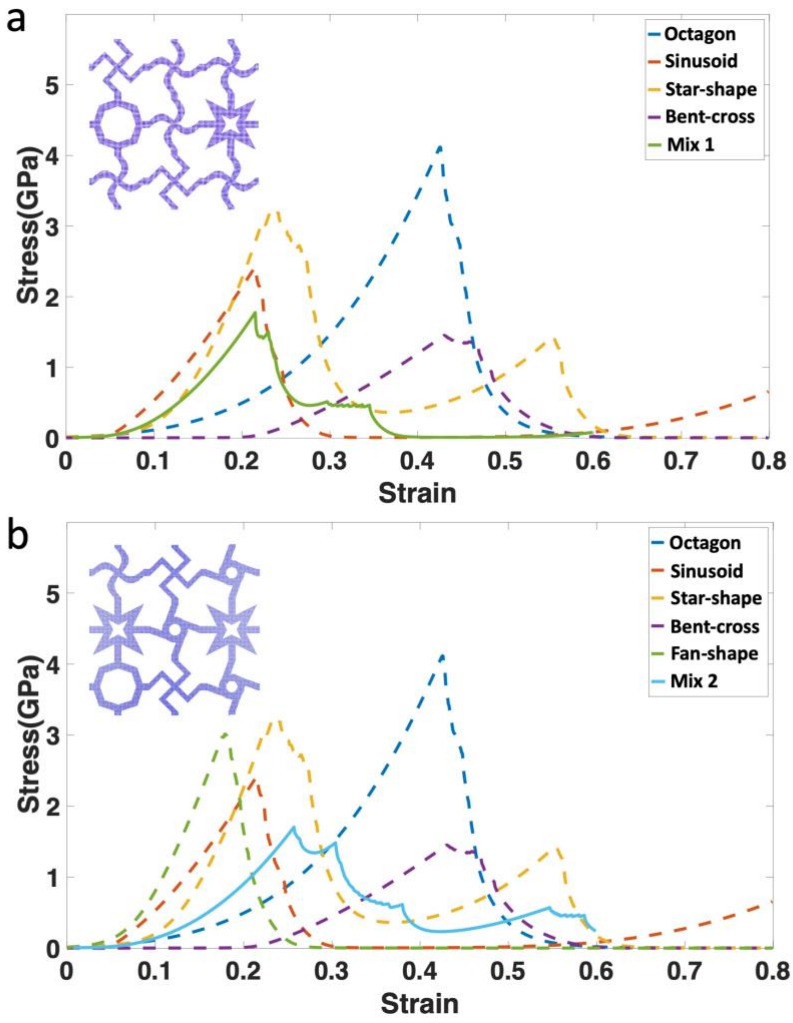


**Figure 3-5** (a) Stress-strain curve comparison between 3x3 homogeneous grid architectured graphene kirigami and heterogeneous grid architectured graphene kirigami sample 1. (b) Stress-strain curve comparison between 3x3 homogeneous grid architectured graphene kirigami and heterogeneous grid architectured graphene kirigami sample 2. Dashed lines represent homogeneous grid graphene kirigami. Solid lines represent heterogeneous grid graphene kirigami.

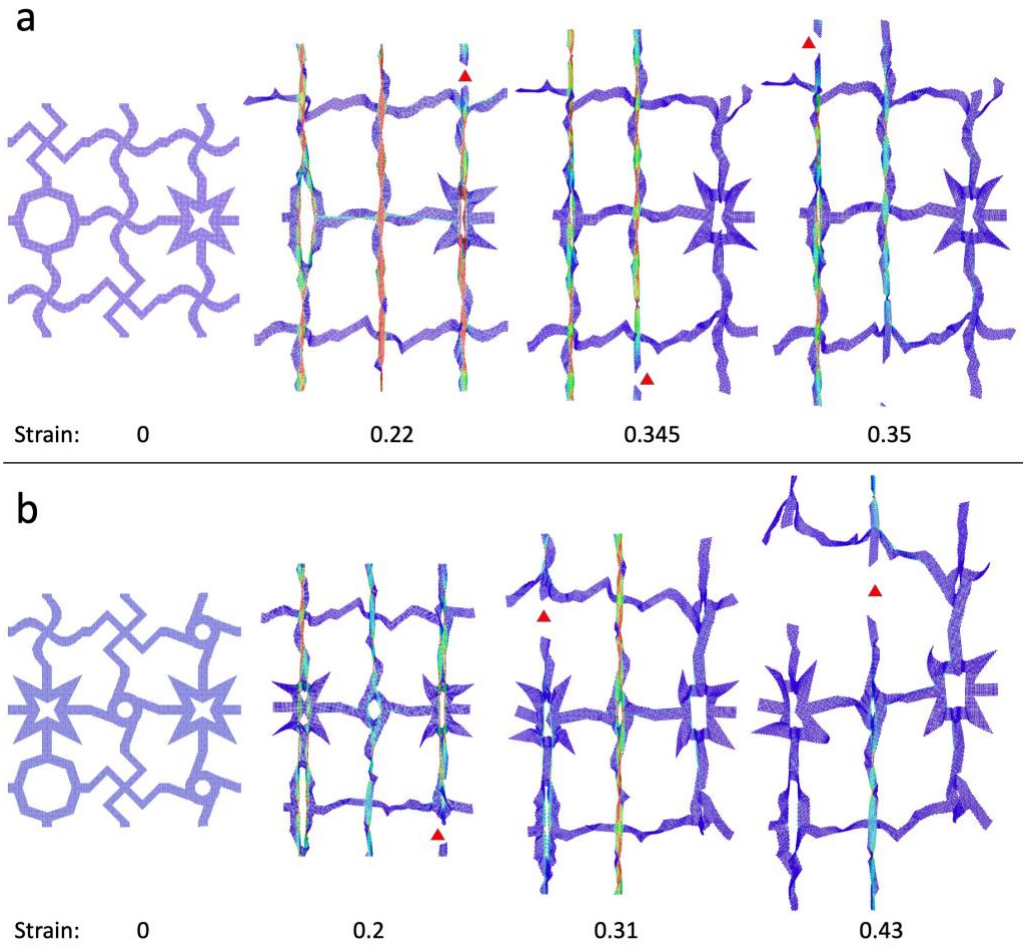


**Figure 3-6** (a) Snapshots of heterogeneous grid architectured graphene kirigami Mix 1 under uniaxial tension. (b) Snapshots of heterogeneous grid architectured graphene kirigami Mix 2 under uniaxial tension.

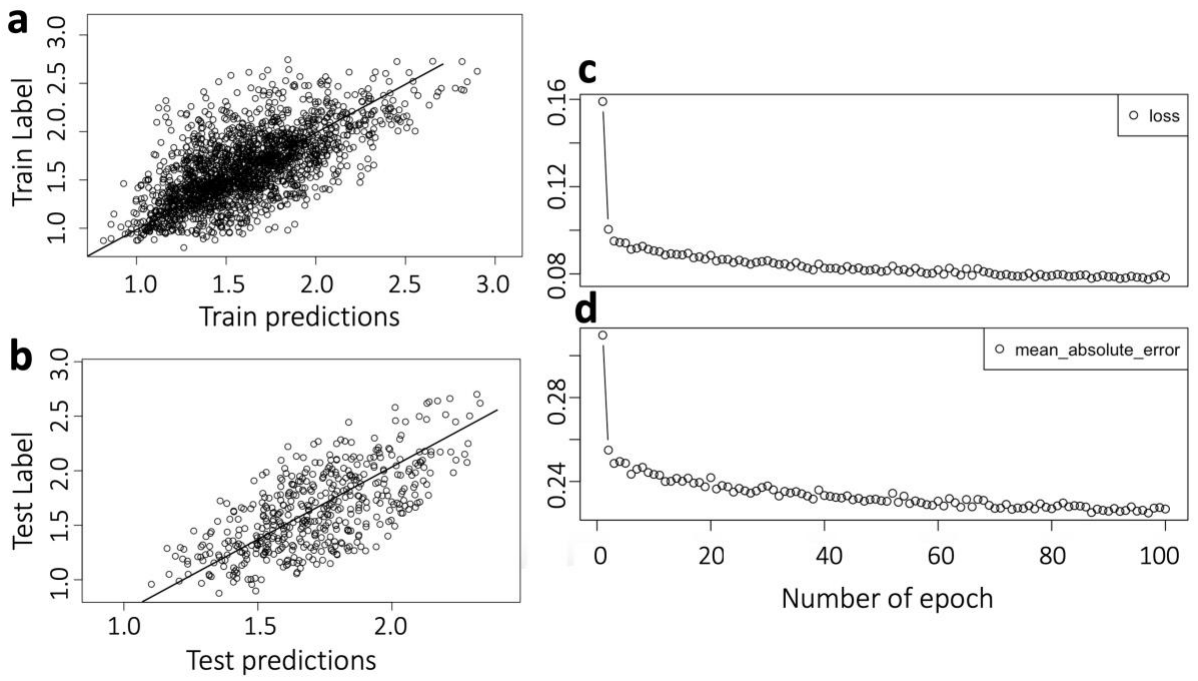


**Figure 3-7** (a) Comparison of the training tensile strength predicted by ML and directly obtained from MD simulation. (b) Comparison of the test tensile strength predicted by ML and directly obtained from MD simulation. (c) The loss error (mean square error) for ML versus number of epochs. (d) The mean absolute error for ML versus number of epochs.

### 3.4 Conclusions

In this chapter, coarse-grained molecular dynamics simulations and BP neural network algorithms have been combined to explore the structure-property relationship of graphene kirigami. Five different cutting patterns have been introduced, namely octagon, fan-shape, sinusoid, bent-cross, and star-shape, while $3 \times 3$ cells have been adopted to construct computational models for graphene kirigami. First, five graphene kirigami samples with homogeneous cutting patterns are tested for their mechanical performance which can be good benchmarks to understand different mechanical characteristics of those cutting patterns. Results indicate that all those cutting patterns share “J-shape” stress-strain curves under uniaxial tension, which can be roughly divided into two stages. In the first stage, the stress increases slowly due to the rigid body motion of the ligands. In the second stage, the stress increases intensively and linearly with strain due to the deformation of

the material itself and the linear elasticity of the material. The mechanical performance of those cutting patterns varies in a wide range, with tensile strength from $1.4\ GPa$ to $4.5\ GPa$ and yield strain ranging from $0.18$ to $0.48$. With those cutting patterns with different mechanical characteristics, graphene kirigami samples with heterogenous cutting patterns are tested for their mechanical performance. Results indicate that the mechanical performance, tensile strength, of graphene kirigami is not necessarily enhanced by introducing strong cutting patterns with high tensile strength. Instead, the tensile strength of graphene kirigami is a result of competition between tensile strength and evolving stiffness with strain of cellular cutting patterns. BP neural network algorithms have been utilized to predict the tensile strength of graphene kirigami with heterogeneous cutting patterns, with tensile strength of cellular patterns as input and tensile strength of graphene kirigami as output. However, the accuracy of the resultant predictions is not good, in which the $R^2$ is around $0.4$. The poor prediction of the BP neural network can be probably attributed to the incomplete information of the input. Including evolving stiffness of cellular cutting patterns could possibly lead to prediction of tensile strength with high precision. Overall, the results of this paper could help deepen the understanding of structure-property relationship of graphene kirigami, providing guidelines for designing and fabricating graphene kirigami with exceptional and tunable mechanical performance.

# CHAPTER4 CONCLUSION AND FUTURE WORK

Recent years have witnessed the explosive researches about metamaterials, such as 2D material kirigami, due to their exceptional mechanical performance such as negative Poisson's ratio, negative stiffness, and outstanding stretchability. In addition to the material itself, the outstanding mechanical properties of 2D material kirigami can be attributed to the unique architected structures. Combining coarse-grained molecular dynamics simulations and machine learning algorithms, I have conducted systematic and comprehensive research to explore the structure-property relationship of graphene kirigami in this thesis. My results deepen the understanding of the relationship between mechanical performance and cutting patterns of graphene kirigami, providing useful guidelines for designing graphene kirigami with exceptional and tunable mechanical performance.

In Chapter 2, my topic mainly focused on how to enhance the mechanical properties and unit cell parameters of 2D materials. I designed different kirigami structures to study the relationship between the geometry of kirigami structures and the mechanical properties of 2D materials, so as to achieve the purpose of enhancing the mechanical properties of 2D materials. I developed a highly transferable CG model to study other 2D materials (graphene, silicene, phosphorene, borophene, and molybdenum disulfide), which further investigated the mechanical properties of different 2D materials under same kirigami structures. The results show two stress-strain behavior patterns, namely J-shaped nonlinearity and linear elasticity, which are dominated by the density of the 2D material kirigami. Specifically, it shows a negative correlation between the width of the kirigami structure and the rotation ability of the ligand, which cause the two different stress-strain

patterns. Based on the results of the five representative kirigami structures that I designed, the ductility (free-stress strain and yield strain) of 2D materials are related to whether the kirigami structure has an inner hole. The kirigami structures with an inner hole show better ductility, notably, and the larger the relative area proportion of inner holes, the better the ductility of the 2D material. The investigation of the mechanical properties of different 2D materials under same kirigami structures show that graphene exhibits higher tensile strength and fracture energy than other materials due to its excellent mechanical properties. In general, my research has broadened the understanding of the relationship between the mechanical performance and structure pattern as well as component material properties for 2D material based cellular kirigami structures, which can provide useful guidance for designing and manufacture of metamaterials with excellent mechanical properties.

In Chapter 3, I further revealed the relationship between the gird architectured kirigami and the mechanical property of 2D materials, I particularly picked graphene as the representative material due to its astonishing mechanical property and studied tensile strength as its representative mechanical property. I still focused on the five architectured kirigami structures that I proposed from Chapter 2 (Octagon, Sinusoid, Bent-cross, Star-shape, Fan-shape) to randomly generate 3 by 3 grid graphene kirigami sheet, and obtained their tensile strength through coarse-grained molecular dynamics simulation. Then, I generated a dataset based on the results, which contain 9 features as predictor variables, in preparation for training the machine learning model. Specifically, I first tested the mechanical properties of five architectured graphene kirigami structures with homogeneous kirigami sheets, which can be used as a good benchmark for understanding the different mechanical characteristics of heterogeneous gird architectured graphene kirigami. Results show that all those homogeneous grid graphene kirigami sheets share “J-shape” stress-

strain curves under uniaxial tension as Chapter 2 observed. The stress increases slowly due to the rigid body motion of the ligands at the beginning, then the stress increases intensively and linearly with strain due to the deformation of the material itself and the linear elasticity of the material. The tensile strength of those homogeneous grid graphene kirigami sheets varies from 1.4 $GPa$ to 4.5 $GPa$ and yield strain varies from 0.18 to 0.48. The wide range of their mechanical properties demonstrate the necessity of learning the heterogeneous gird architectured graphene kirigami, which is subsequently tested.

Results also indicate that the tensile strength of graphene kirigami is a result of competition between tensile strength and evolving stiffness with strain of cellular cutting patterns, which means that the architectured structures with high tensile strength do not play the leading role in the tensile strength of the whole heterogeneous gird architectured graphene kirigami. I next performed a machine learning model through BP neural network algorithm to predict the tensile strength of heterogeneous gird architectured graphene kirigami. The dataset can be divided to two parts: one is the input, which contains tensile strength of cellular patterns as predictor, another part is the tensile strength of heterogeneous gird architectured graphene kirigami as output. However, due to the incomplete information of the input and the lack of the training data points, the accuracy of the resultant predictions still needs to be improved. Result shows the R2 increased up to 0.4 by improving the structural details of the input dataset, which provide a possible way to improve the precision of the prediction by evolving stiffness of cellular cutting pattern. Overall, the results of this paper could help expand the understanding of structure-property relationship of architectured graphene kirigami, providing guidelines for designing and predicting architectured graphene kirigami.

With respect to future research, the following hypotheses will be tested:

Hypothesis #1: Compared with back propagation neural networks, convolution neural networks are a robust and accurate tool to predict the relationship between cutting patterns and mechanical performance of 2D material kirigami.

Hypothesis #2: Genetic algorithms can be combined with machine learning algorithms to optimize the cutting patterns of graphene kirigami to achieve exceptional mechanical performance.

To test those two hypotheses, convolutional neural network algorithms will be adopted to predict the mechanical performance of graphene kirigami based on initial architected structures of graphene kirigami. Binary pictures of graphene kirigami will be used as input while the mechanical performance of graphene kirigami will be used as output. Datasets above will be used to train the convolutional neural network to obtain the structure-property relationship with high precision for graphene kirigami. Moreover, combined with genetic algorithms, convolutional neural network algorithms will be further utilized to optimize cutting patterns of graphene kirigami to achieve outstanding mechanical performance. The genetic algorithms are a stochastic search-based metaheuristic method for searching optimal solution by mimicking the processing of biological reproduction and the theory of evolution. Genetic algorithms can identify the optimal design for tessellating materials with a small amount of sampling size by using fitness ranking and diversity. The method proposed here can also easily be extended to study larger systems or a hierarchical structural material system.

REFERENCES


1. H Zhang, *ACS Nano*. *9*, 9451-9469 (2015).

2. Y Cui, X Duan, J Hu, C M Lieber, *The Journal of Physical Chemistry B*. *104*, 5213-5216 (2000).

3. M S Dresselhaus, G Dresselhaus, P C Eklund, A M Rao, Carbon Nanotubes. In *The Physics of Fullerene-Based and Fullerene-Related Materials*, Andreoni, W., Ed. Springer Netherlands: Dordrecht, 2000; pp 331-379.

4. K S Novoselov, A K Geim, S V Morozov, D Jiang, Y Zhang, S V Dubonos, I V Grigorieva, A A Firsov, *Science*. *306*, 666 (2004).

5. P Vogt, P De Padova, C Quaresima, J Avila, E Frantzeskakis, M C Asensio, A Resta, B Ealet, G Le Lay, *Physical Review Letters*. *108*, 155501 (2012).

6. S Gadipelli, Z X Guo, *Progress in Materials Science*. *69*, 1-60 (2015).

7. J F Gregg, W Allen, K Ounadjela, M Viret, M Hehn, S M Thompson, J M D Coey, *Physical Review Letters*. *77*, 1580-1583 (1996).

8. C M Varma, *Physical Review B*. *54*, 7328-7333 (1996).

9. S Manzeli, D Ovchinnikov, D Pasquier, O V Yazyev, A Kis, *Nature Reviews Materials*. *2*, 17033 (2017).

10. R Fei, W Li, J Li, L Yang, *Applied Physics Letters*. *107*, 173104 (2015).

11. P A Miller, G A Hebner, K E Greenberg, P D Pochan, B P Aragon, *J Res Natl Inst Stand Technol*. *100*, 427-439 (1995).

12. S O Koswatta, A Valdes-Garcia, M B Steiner, Y Lin, P Avouris, *IEEE Transactions on Microwave Theory and Techniques*. *59*, 2739-2750 (2011).

13. S Pang, Y Hernandez, X Feng, K Müllen, *Advanced Materials*. *23*, 2779-2795 (2011).

14. C Il-Joo, S Taeksang, B Sang-Hyun, Y Euisik, *IEEE Transactions on Microwave Theory and Techniques*. *53*, 2450-2457 (2005).

15. O K Varghese, M Paulose, C A Grimes, *Nature Nanotechnology*. *4*, 592-597 (2009).

16. K C Divya, J Østergaard, *Electric Power Systems Research*. *79*, 511-520 (2009).

17. P H Siegel, *IEEE Transactions on Microwave Theory and Techniques*. *50*, 910-928 (2002).

18. B W H Baugher, H O H Churchill, Y Yang, P Jarillo-Herrero, *Nature Nanotechnology*. *9*, 262-267 (2014).

19. M Xu, T Liang, M Shi, H Chen, *Chemical Reviews*. *113*, 3766-3798 (2013).

20. M K Blees, A W Barnard, P A Rose, S P Roberts, K L McGill, P Y Huang, A R Ruyack, J W Kevek, B Kobrin, D A Muller, P L McEuen, *Nature*. *524*, 204-207 (2015).

21. R M Neville, A Monti, K Hazra, F Scarpa, C Remillat, I R Farrow, *Composite Structures*. *114*, 30-40 (2014).

22. Y Jiang, Z Liu, N Matsuhisa, D Qi, W R Leow, H Yang, J Yu, G Chen, Y Liu, C Wan, Z Liu, X Chen, *Advanced Materials*. *30*, 1706589 (2018).

23. N Liu, M Becton, L Zhang, K Tang, X Wang, *Nanoscale Advances*. *1*, 2891-2900 (2019).

24. T A M Hewage, K L Alderson, A Alderson, F Scarpa, *Advanced Materials*. *28*, 10323-10332 (2016).

25. T Klatt, M R Haberman, *Journal of Applied Physics*. *114*, 033503 (2013).

26. P Z Hanakata, Z Qi, D K Campbell, H S Park, *Nanoscale*. *8*, 458-463 (2016).

27. Z Qi, D K Campbell, H S Park, *Physical Review B*. *90*, 245437 (2014).

28. H Fu, K Nan, W Bai, W Huang, K Bai, L Lu, C Zhou, Y Liu, F Liu, J Wang, M Han, Z Yan, H Luan, Y Zhang, Y Zhang, J Zhao, X Cheng, M Li, J W Lee, Y Liu, D Fang, X Li, Y Huang, Y Zhang, J A Rogers, *Nat. Mater*. *17*, 268-276 (2018).

29. W Yang, Q Liu, Z Gao, Z Yue, B Xu, *Proceedings of the National Academy of Sciences*. *115*, E7245 (2018).

30. W Yang, Q Liu, Z Gao, Z Yue, B Xu, *Proceedings of the National Academy of Sciences*. *115*, E7245-E7254 (2018).

31. C Coulais, E Teomy, K de Reus, Y Shokef, M van Hecke, *Nature*. *535*, 529-532 (2016).

32. B Florijn, C Coulais, M van Hecke, *Physical Review Letters*. *113*, 175503 (2014).

33. M J Mirzaali, R Hedayati, P Vena, L Vergani, M Strano, A A Zadpoor, *Applied Physics Letters*. *111*, 051903 (2017).

34. J L Silverberg, A A Evans, L McLeod, R C Hayward, T Hull, C D Santangelo, I Cohen, *Science*. *345*, 647-650 (2014).

35. J A Burg, M S Oliver, T J Frot, M Sherwood, V Lee, G Dubois, R H Dauskardt, *Nature Communications*. *8*, 1019 (2017).

36. J W Rocks, N Pashine, I Bischofberger, C P Goodrich, A J Liu, S R Nagel, *Proceedings of the National Academy of Sciences*. *114*, 2520-2525 (2017).

37. L Yan, R Ravasio, C Brito, M Wyart, *Proceedings of the National Academy of Sciences*. *114*, 2526-2531 (2017).

38. Y Liu, T Zhao, W Ju, S Shi, *Journal of Materiomics*. *3*, 159-177 (2017).

39. D H Bailey, R Barrio, J M Borwein, *Applied Mathematics and Computation*. *218*, 10106-10121 (2012).

40. Y Saad, J R Chelikowsky, S M Shontz, *SIAM Review*. *52*, 3-54 (2010).

41. I G Tironi, R Sperb, P E Smith, W F van Gunsteren, *The Journal of Chemical Physics*. *102*, 5451-5459 (1995).

42. K A Fichthorn, W H Weinberg, *The Journal of Chemical Physics*. *95*, 1090-1096 (1991).

43. G Caginalp, P Fife, *Physical Review B*. *33*, 7792-7794 (1986).

44. Z Xu, C Gao, *Accounts of Chemical Research*. *47*, 1267-1276 (2014).

45. N Wagner, J M Rondinelli, *Frontiers in Materials*. *3*, (2016).

46. R M Neville, F Scarpa, A Pirrera, *Scientific Reports*. *6*, 31067 (2016).

47. J A Fan, W-H Yeo, Y Su, Y Hattori, W Lee, S-Y Jung, Y Zhang, Z Liu, H Cheng, L Falgout, M Bajema, T Coleman, D Gregoire, R J Larsen, Y Huang, J A Rogers, *Nature Communications*. *5*, 3266 (2014).

48. A Miyamoto, S Lee, N F Cooray, S Lee, M Mori, N Matsuhisa, H Jin, L Yoda, T Yokota, A Itoh, M Sekino, H Kawasaki, T Ebihara, M Amagai, T Someya, *Nature Nanotechnology*. *12*, 907-913 (2017).

49. S Xu, Y Zhang, J Cho, J Lee, X Huang, L Jia, J A Fan, Y Su, J Su, H Zhang, H Cheng, B Lu, C Yu, C Chuang, T-i Kim, T Song, K Shigeta, S Kang, C Dagdeviren, I Petrov, P V Braun, Y Huang, U Paik, J A Rogers, *Nature Communications*. *4*, 1543 (2013).

50. D Mousanezhad, S Babaee, R Ghosh, E Mahdi, K Bertoldi, A Vaziri, *Physical Review B*. *92*, 104304 (2015).

51. Y Chen, T Li, F Scarpa, L Wang, *Physical Review Applied*. *7*, 024012 (2017).

52. P Z Hanakata, E D Cubuk, D K Campbell, H S Park, *Physical Review Letters*. *121*, 255304 (2018).

53. M Gamil, Q X Pei, Y Y Zhang, *Computational Materials Science*. *173*, 109462 (2020).

54. Z Liu, H Du, J Li, L Lu, Z-Y Li, N X Fang, *Science Advances*. *4*, eaat4436 (2018).

55. L Ruiz, W Xia, Z Meng, S Keten, *Carbon*. *82*, 103-115 (2015).

56. B Arash, H S Park, T Rabczuk, *Composite Structures*. *134*, 981-988 (2015).

57. M Li, Y-Z Gu, H Liu, Y-X Li, S-K Wang, Q Wu, Z-G Zhang, *Composites Science and Technology*. *86*, 117-121 (2013).

58. Z Meng, R A Soler-Crespo, W Xia, W Gao, L Ruiz, H D Espinosa, S Keten, *Carbon*. *117*, 476-487 (2017).

59. R E Rudd, J Q Broughton, *Physical Review B*. *58*, R5893-R5896 (1998).

60. N Liu, M Becton, L Zhang, H Chen, X Zeng, R Pidaparti, X Wang, *Physical Chemistry Chemical Physics*. *21*, 1884-1894 (2019).

61. S Cranford, D Sen, M J Buehler, *Applied Physics Letters*. *95*, 123121 (2009).

62. H Zhong, K Huang, G Yu, S Yuan, *Physical Review B*. *98*, 054104 (2018).

63. J-W Jiang, *Nanotechnology*. *26*, 315706 (2015).

64. R E Roman, S W Cranford, *Computational Materials Science*. *82*, 50-55 (2014).

65. N Liu, J Hong, R Pidaparti, X Wang, *Nanoscale*. *8*, 5728-5736 (2016).

66. Z Wang, T-Y Lü, H-Q Wang, Y P Feng, J-C Zheng, *Physical Chemistry Chemical Physics*. *18*, 31424-31430 (2016).

67. Q Wei, X Peng, *Applied Physics Letters*. *104*, 251915 (2014).

68. Y Li, P Chen, H Liu, J Peng, F Gao, N Luo, *Physical Chemistry Chemical Physics*. *21*, 19115-19125 (2019).

69. S Xiong, G Cao, *Nanotechnology*. *27*, 105701 (2016).

70. A K Rappe, C J Casewit, K S Colwell, W A Goddard, W M Skiff, *Journal of the American Chemical Society*. *114*, 10024-10035 (1992).

71. K Weiss, J M Phillips, *Physical Review B*. *14*, 5392-5395 (1976).

72. S Plimpton, *Journal of Computational Physics*. *117*, 1-19 (1995).

73. A Stukowski, *Modelling and Simulation in Materials Science and Engineering*. *18*, 015012 (2010).

74. V S Deshpande, N A Fleck, M F Ashby, *Journal of the Mechanics and Physics of Solids*. *49*, 1747-1769 (2001).

75. N Winter, M Becton, L Zhang, X Wang, *Acta Materialia*. *124*, 127-136 (2017).

76. L C Montemayor, J R Greer, *Journal of Applied Mechanics*. *82*, (2015).

77. N A Fleck, V S Deshpande, M F Ashby, *Proceedings of the Royal Society A: Mathematical, Physical and Engineering Sciences*. *466*, 2495-2516 (2010).

78. T A Schaedler, A J Jacobsen, A Torrents, A E Sorensen, J Lian, J R Greer, L Valdevit, W B Carter, *Science*. *334*, 962-965 (2011).

79. T Abbas, I Kavrakov, G Morgenthal, T Lahmer, *Computers & Structures*. *231*, (2020).

80. W Qin, X Li, W-W Bian, X-J Fan, J-Y Qi, *Biomaterials*. *31*, 1007-1016 (2010).

81. J Wan, J-W Jiang, H S Park, *Carbon*. *157*, 262-269 (2020).

82. S Fan, X Wang, S Yang, *International Journal of Pattern Recognition and Artificial Intelligence*. *34*, 2058007 (2019).

83. A R Sanabria, J Ye, *Pervasive and Mobile Computing*. *64*, 101147 (2020).

# APPENDIX A

## Supplemental Materials for Chapter 2

## MECHANICS OF 2D MATERIALS BASED CELLULAR KIRIGAMI STRUCTURES: A COMPUTATIONAL STUDY[1]

[1]Shaoheng Li*, Ning Liu, Matthew Becton, Nicholas Winter, Ramana M. Pidaparti, Xianqiao Wang, 2020, "Mechanics of 2D materials based cellular kirigami structures: A computational study", JOM. Reprinted here with permission of publisher.

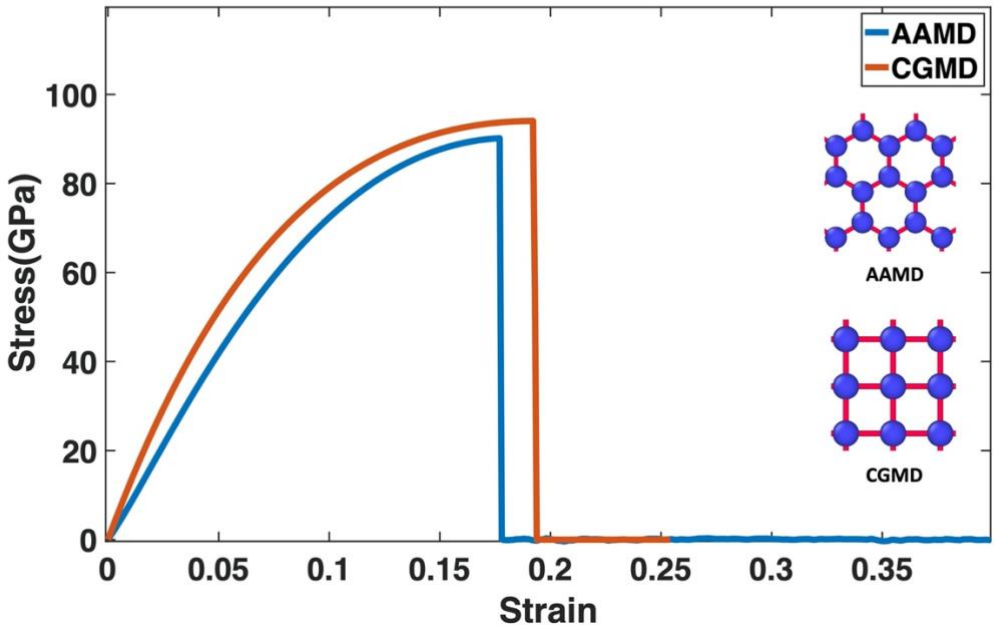


**Figure A-1** Comparison of stress-strain responses of a graphene sheet from all-atom molecular dynamics (AAMD) simulations and coarse-grained molecular dynamics (CGMD) simulations.

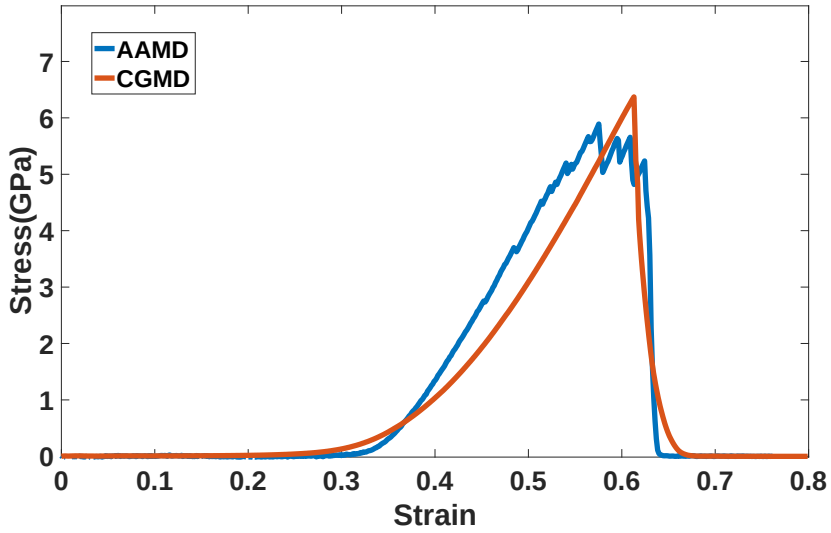


**Figure A-2** Comparison of stress-strain responses of graphene-based octagonal cell deformation from all-atom molecular dynamics (AAMD) simulations and coarse-grained molecular dynamics (CGMD) simulations.

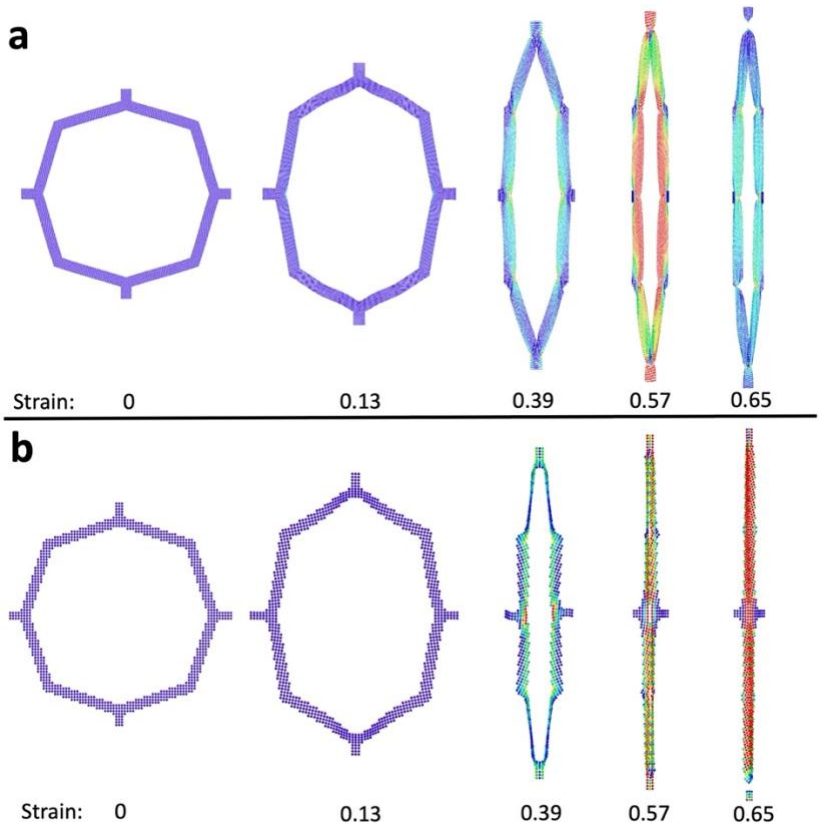


**Figure A-3** (a)Snapshots of graphene-based AAMD octagonal cell deformation. (b)Snapshots of graphene-based CGMD graphene based octagonal cell deformation.

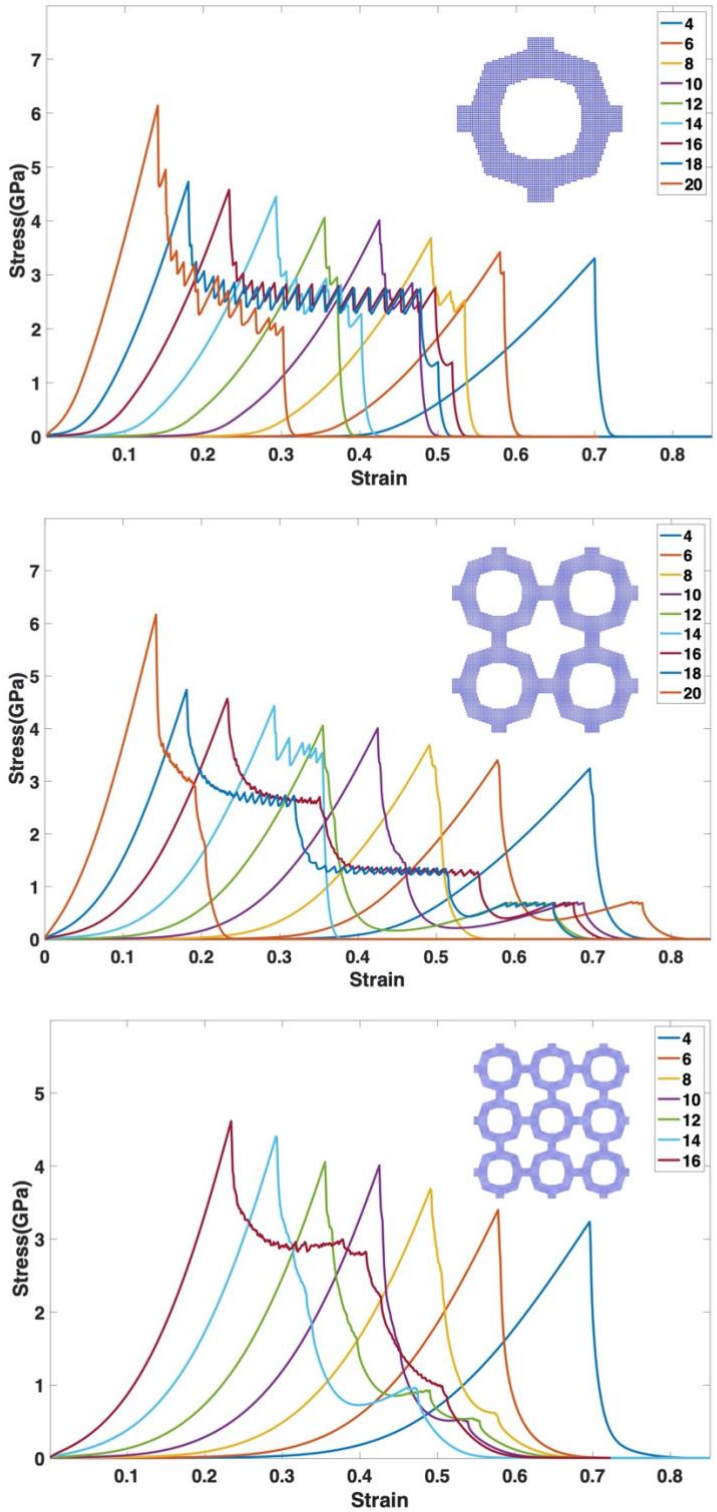


**Figure A-4** Stress-strain curve of different numbers of octagonal unit cell tiles (1×1; 2×2; 3×3).

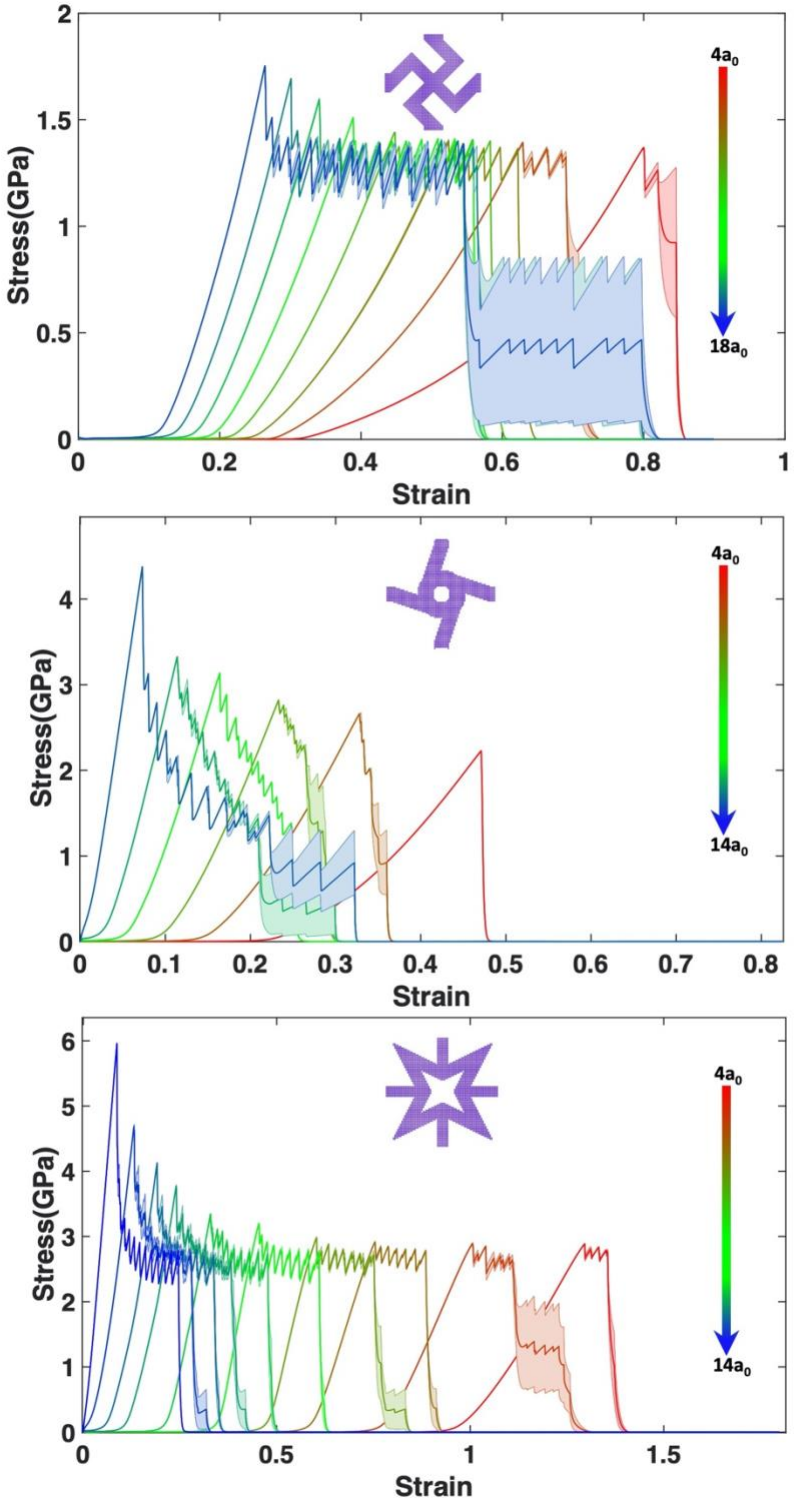


**Figure A-5** Stress-strain curve of bent-cross, fan, and star patterns.

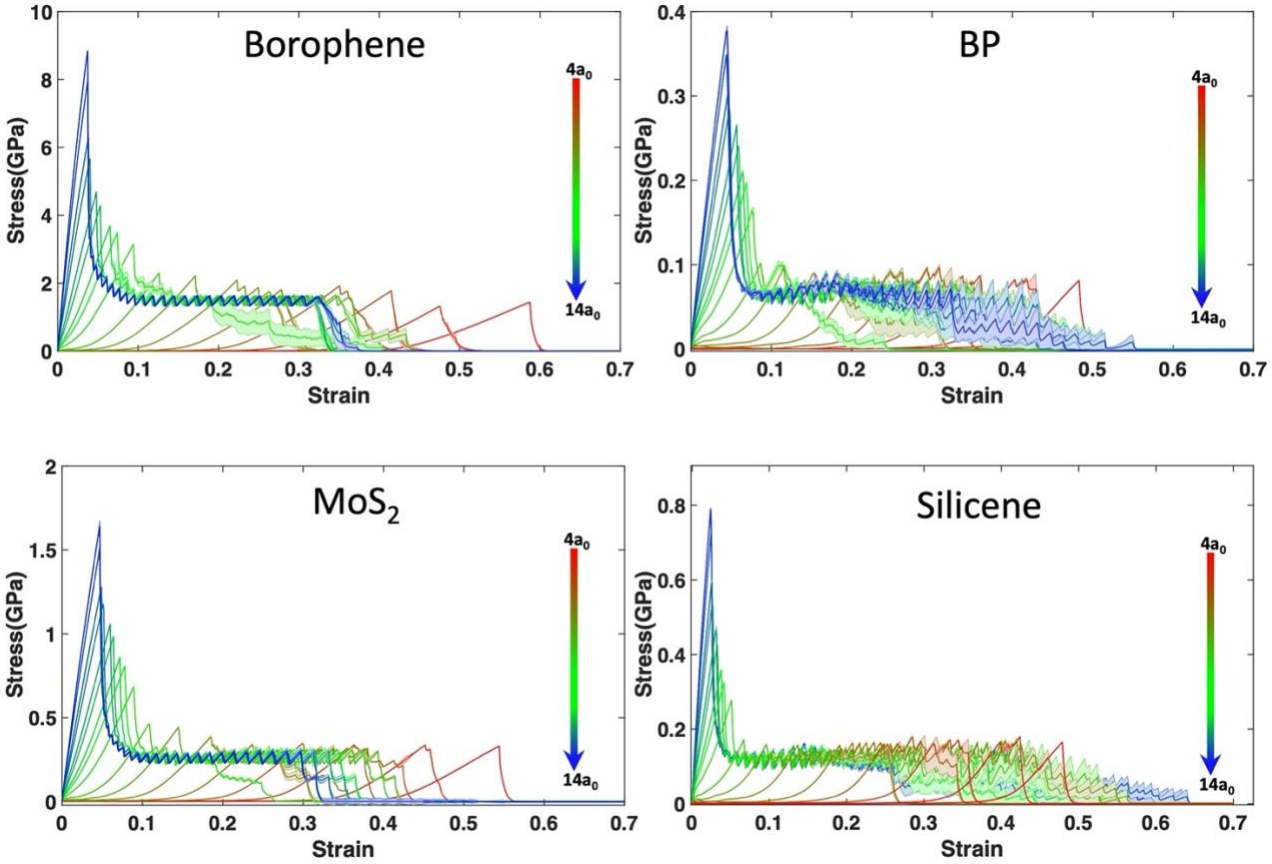


**Figure A-6** Stress-strain curve of octagonal cells made of four different materials, namely Borophene, BP, $MoS_2$, and Silicene.

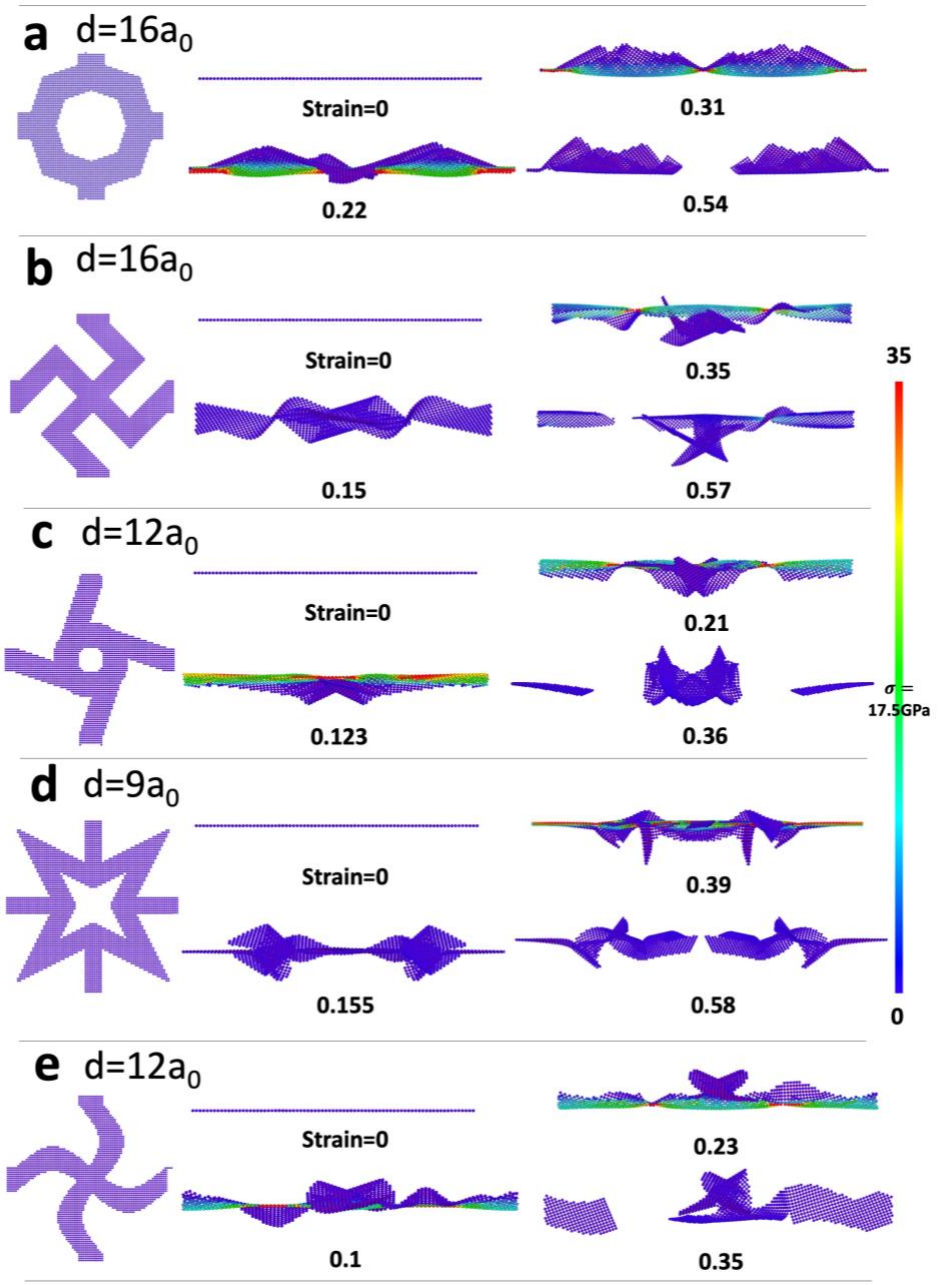


**Figure A-7** (a)Snapshot of octagonal cell out-of-plane deformation. (b)Snapshot of bent-cross cell out-of-plane deformation. (c)Snapshot of fan cell out-of-plane deformation. (d)Snapshot of star cell out-of-plane deformation. (e)Snapshot of sinusoidal cell out-of-plane deformation. (The snapshots are picked out in the same manner as described in Figure 2-3)

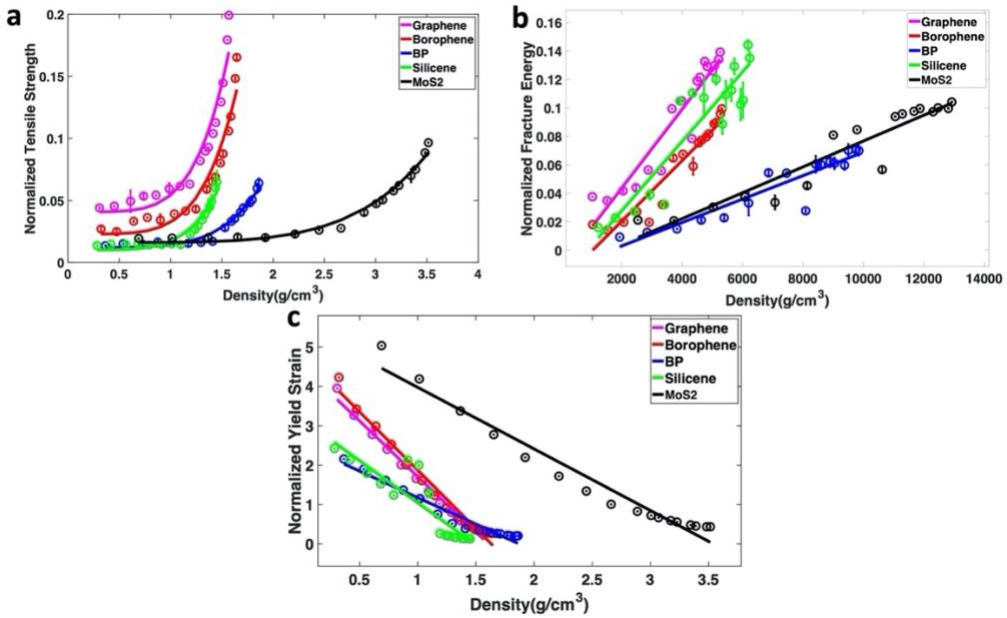


**Figure A-8** The normalized mechanical properties as a function of density: (a) normalized tensile strength; (b) normalized fracture energy; (c) normalized yield strain.